Influence of Shear Heating and Thermomechanical Coupling on Earthquake Sequences and the Brittle-Ductile Transition

Kali Allison[1] and Eric M Dunham[2]

[1]University of Maryland
[2]Stanford University

November 23, 2022

Abstract

Localized frictional sliding on faults in the continental crust transitions at depth to distributed deformation in viscous shear zones. This brittle-ductile transition (BDT), and/or the transition from velocity-weakening (VW) to velocity-strengthening (VS) friction, are controlled by the lithospheric thermal structure and composition. Here we investigate these transitions, and their effect on the depth extent of earthquakes, using 2D antiplane shear simulations of a strike-slip fault with rate-and-state friction. The off-fault material is viscoelastic, with temperature-dependent dislocation creep. We solve the heat equation for temperature, accounting for frictional and viscous shear heating that creates a thermal anomaly relative to the ambient geotherm which reduces viscosity and facilitates viscous flow. We explore several geotherms and effective normal stress distributions (by changing pore pressure), quantifying the thermal anomaly, seismic and aseismic slip, and the transition from frictional sliding to viscous flow. The thermal anomaly can reach several hundred degrees below the seismogenic zone in models with hydrostatic pressure, but is smaller for higher pressure (and these high-pressure models are most consistent with San Andreas Fault heat flow constraints). Shear heating raises the BDT, sometimes to where it limits rupture depth rather than the frictional VW-to-VS transition. Our thermomechanical modeling framework can be used to evaluate lithospheric rheology and thermal models through predictions of earthquake ruptures, postseismic and interseismic crustal deformation, heat flow, and the geological structures that reflect the complex deformation beneath faults.

Influence of Shear Heating and Thermomechanical Coupling on Earthquake Sequences and the Brittle-Ductile Transition

Kali L. Allison[1,2], **Eric M. Dunham**[1,3]

[1]Department of Geophysics, Stanford University, Stanford, California, USA
[2]now at: Department of Geology, University of Maryland, College Park, Maryland, USA
[3]Institute for Computational and Mathematical Engineering, Stanford University, Stanford, California, USA

Key Points:

- Earthquake modeling predicts viscous shear zones a few kilometers wide below faults
- Shear heating creates a thermal anomaly of tens to hundreds of degrees in the lower crust
- Shear heating raises the brittle-ductile transition and can limit rupture depth

Corresponding author: Kali L. Allison, kalliso1@umd.edu

Abstract

Localized frictional sliding on faults in the continental crust, typically occurring in earthquakes, transitions at depth to more broadly distributed deformation in viscous shear zones. This brittle-ductile transition (BDT), and/or the transition from velocity-weakening (VW) to velocity-strengthening (VS) friction at depth, are controlled by the thermal structure and composition of the lithosphere. Here we investigate this transition, and its effect on the depth extent of earthquake ruptures, using 2D antiplane shear earthquake sequence simulations of a vertical strike-slip fault with rate-and-state friction. The off-fault material is viscoelastic, with a temperature-dependent, power-law dislocation creep flow law. We simultaneously solve the heat equation for temperature, accounting for frictional and viscous shear heating that creates a thermal anomaly (i.e., temperatures in excess of the ambient geotherm) which reduces effective viscosity and facilitates viscous flow. We explore a range of ambient geotherms and fault effective normal stress distributions (by changing the pore pressure gradient), quantifying the thermal anomaly, patterns of seismic and aseismic slip, and the nature of the transition from frictional sliding to viscous flow. The thermal anomaly, which has significant contributions from both frictional and viscous shear heating, can reach several hundred degrees just below the seismogenic zone in models with hydrostatic pore pressure, but is smaller in models with higher pore pressure (and these latter models are most consistent with surface heat flow constraints from the San Andreas Fault). Shear heating raises the BDT, sometimes to the point where it limits rupture depth rather than the frictional VW-to-VS transition. Our fully coupled thermomechanical earthquake sequence modeling framework can be used to evaluate proposed lithospheric rheology and thermal models through model predictions of earthquake ruptures, postseismic and interseismic crustal deformation, heat flow, and the geological structures that reflect the complex nature of deformation beneath faults.

1 Introduction

Thermal structure plays a major role in the rheology and dynamics of the continental lithosphere and active faults embedded within it. Increasing temperature with depth activates crystal-plastic creep, also called viscous flow, producing the well-known transition from localized frictional sliding across faults (i.e., brittle deformation) to viscous flow (i.e., ductile deformation) (e.g., Byerlee, 1978; Goetze & Evans, 1979; Brace & Kohlstedt, 1980; Sibson, 1982, 1984). Below the brittle-ductile transition (BDT), crystal-plastic creep reduces the flow stress of lithospheric rocks, preventing seismic slip and producing a zone of viscous deformation that forms the ductile root of faults. Temperature also influences the frictional properties of faults, with many experiments providing evidence for a transition from steady-state velocity-weakening to velocity-strengthening friction as temperature is increased, as reviewed by Hu & Sun (2020). Experiments suggest that granite and related crustal rocks undergo this transition at roughly 350 °C (e.g., Dieterich, 1978; Ruina, 1983; Tullis & Weeks, 1986; Blanpied et al., 1991, 1995; Chester, 1995; Aharonov & Scholz, 2018, 2019), though other experiments suggest that these rocks can remain velocity-weakening up to 600 °C (Mitchell et al., 2016). The velocity-weakening portion of a fault can host earthquakes, while velocity-strengthening portions generally slip aseismically. Both the brittle-ductile transition and the frictional stability transition have the potential to affect the extent of the seismogenic zone and the depth to which large ruptures will propagate. Furthermore, due to the temperature-dependence of viscous flow, the depth of the BDT can be altered by frictional and viscous shear heating, which produces a thermal anomaly (i.e., temperature deviation from the ambient geotherm) within and around fault zones. A variety of observations, on both active and exhumed faults, provide insight into the extent of the heat generation and its effect on the structure and dynamics of faults and their roots.

Field observations of exhumed seismogenic zones of faults reveal that, while the overall fault zone in the upper crust may be hundreds of meters wide, slip during individual earthquakes might be localized onto narrow zones that are just tens of microns to centimeters wide (e.g., Chester & Chester, 1998; Wibberley & Shimamoto, 2002; Sibson, 2003; Chester et al., 2004; Noda & Shimamoto, 2005; Rice, 2006). As temperature increases with depth, this highly localized, brittle deformation style ultimately transitions into more distributed viscous deformation in the form of relatively broad mylonite zones. Seismic imaging and seismicity studies of active faults, as well as geologic studies of exhumed fault zones, reveal a rich array of deformation styles and degree of localization in the middle and lower crust and upper mantle. Many continental transform faults persist as highly localized features to the Moho or even below it, such as the San Andreas and San Jacinto Faults (Lemiszki & Brown, 1988; Henstock et al., 1997; Zhu, 2000; Vauchez & Tommasi, 2003; Lekic et al., 2011; Miller et al., 2014) and the Newport-Inglewood Fault (Inbal et al., 2016). Others, including the Dead Sea, Alpine, and Wairau Faults, apparently transition into distributed zones of deformation in the lower crust (Klosko et al., 1999; Molnar, 1999; Weber et al., 2004). Some major exhumed mylonite zones from the lower crust, such as the Great Slave Lake shear zone, the South Amorican shear zone, and the Woodroffe Thrust mylonite zone (Bell, 1978; Berthe et al., 1979; Weijermars, 1987; Camacho et al., 1995; Hanmer, 1988), can be tens of kilometers in width. However, because the upper crustal fault zone has eroded away, it is not clear if these zones are the result of a single fault broadening into a shear zone, or the lower crustal signature of a zone of anastomosing faults in the brittle crust above (Norris & Cooper, 2003). Other exhumed mylonite zones are relatively narrow, such as the 1 to 2-km-wide mylonite zone from the middle and lower crust beneath the Alpine Fault (Norris & Cooper, 2003; Norris & Toy, 2014) and the 2-km-wide mylonite zone in the Salzach–Ennstal–Mariazell–Puchberg Fault system (Rosenberg & Schneider, 2008; Frost et al., 2011). Some exhumed fault zones have features such as mutually overprinted pseudotachylyte and mylonite that are interpreted as evidence for rupture propagation below the BDT (e.g., Vissers et al., 1997; Sibson & Toy, 2006; Lin et al., 2005; Cole et al., 2007; Griffith et al., 2008; Frost et al., 2011; White, 2012; Kirkpatrick & Rowe, 2013; Melosh et al., 2018; Petley-Ragan et al., 2019).

These transitions in deformation style with depth are also reflected in the strength profiles of the lithosphere. The lithosphere is typically divided into three layers: the upper crust, lower crust, and upper mantle. The upper crust is brittle, so its strength is determined by the frictional strength of faults. The transition to viscous flow generally occurs in the lower crust or upper mantle, with their strength depending on their composition, water content and presence of partial melt, and the strain rate of deformation. The continental lithosphere near transform faults may be best described by the "crème brûlée" model, in which the upper mantle is weaker than the lower crust (e.g., Maggi et al., 2000; Jackson, 2002; Bürgmann & Dresen, 2008). This model is supported, in regions such as the Mojave Desert in southern California, by estimates of the rheological structure from exhumed xenoliths and transient postseismic deformation (e.g., Johnson et al., 2007; Thatcher & Pollitz, 2008; Behr & Hirth, 2014; Behr & Platt, 2014; Chatzaras et al., 2015). Other observations also support this view of a weak upper mantle. Behr & Platt (2014) created a global compilation of shear stress measurements from exhumed large-scale ductile shear zones and active faults, and found that the middle crust at and below the BDT is the main load-bearing layer in the lithosphere. They also found that the brittle upper crust was relatively weak. Many of their lowest estimates for fault strength come from mature faults such as the San Andreas and Denali Faults, indicating that mature faults may be weak (Behr & Platt, 2014). It may be that the continental lithosphere cannot be reduced to a simple layered model like the "crème brûlée" model, and that lateral variations in rheology must be accounted for (e.g., Bürgmann & Dresen, 2008; Jackson et al., 2008; Wright et al., 2013). In particular, the strength of the crust and mantle may be significantly reduced in the vicinity of major faults as a result of weakening mechanisms such as shear heating and grain-size reduction, and as a result one must take

care in interpreting postseismic deformation (Bürgmann & Dresen, 2008; Wright et al., 2013).

One avenue of research that synthesizes many of these observations is the simulation of sequences of earthquake and aseismic slip, in which the coseismic, postseismic, and interseismic phases of the earthquake cycle are modeled within a single simulation framework. Many such studies have focused on faults with rate-and-state friction in linear elastic half-spaces (e.g., Tse & Rice, 1986; Rice, 1993; Lapusta et al., 2000; Kaneko et al., 2011; Erickson & Dunham, 2014). These models can be calibrated to match coseismic, postseismic, and interseismic observations (Barbot et al., 2012). Other earthquake cycle studies have utilized viscoelastic bulk rheologies but with kinematically imposed earthquakes (e.g., Savage & Prescott, 1978; Thatcher, 1983; Thatcher & England, 1998; Johnson et al., 2007; Takeuchi & Fialko, 2012; Zhang & Sagiya, 2017). A few models fully couple rate-and-state friction and a linear or power-law viscoelastic bulk rheology. Some consider a fault-containing elastic layer over a viscoelastic half-space (Kato, 2002; Lambert & Barbot, 2016a). Others simulate only a single event rather than multiple cycles (Barbot & Fialko, 2010; Aagaard et al., 2013). An alternative approach was taken by Shimamoto & Noda (2014) and Beeler et al. (2018), who captured the frictional sliding to viscous flow transition through a unified constitutive law applied on an "interface" in an otherwise elastic solid. This approach is based on the assumption that viscous flow is confined to a ductile fault root whose width (which must be specified a priori) is far less other length scales of interest. Most recently, in Allison & Dunham (2018), we developed a method for simulating earthquake sequences on a rate-and-state frictional fault embedded within a viscoelastic solid. The transition from fault slip to viscous flow, and the width of the fault root, are determined as part of the solution, and can vary spatially and temporally, unlike the methods reviewed above. Miyake & Noda (2019) have also coupled rate-and-state friction with bulk viscoelasticity, exploring how viscous stress relaxation can alter or suppress slip as the Maxwell time approaches or becomes smaller than the earthquake recurrence interval. However, their spectral boundary integral equation method is limited to homogeneous, linear viscoelastic solids, so cannot capture the depth-dependent transitions that comprise the focus of Allison & Dunham (2018) and our current study.

A few studies have considered frictional and viscous shear heating, and the associated thermal anomaly, in the context of earthquake cycles. Models which include only viscous shear heating, and use the geometry of a fault-containing layer over a viscoelastic half-space, provide the following estimates of thermal anomaly: 1-20 °C (Lyzenga et al., 1991; Savage & Lachenbruch, 2003) or up to a few hundred °C (Thatcher & England, 1998; Leloup et al., 1999; Takeuchi & Fialko, 2012; Moore & Parsons, 2015). We note that Lyzenga et al. (1991) use a weak viscous rheology that places the BDT at only 7 km depth (for a high stress fault model and power-law flow, similar to our model) and reduces shear heating by about an order of magnitude, relative to other studies, at a given stress level. The low thermal anomaly estimate of Savage & Lachenbruch (2003) stems from their choice of friction coefficient < 0.1; adjusting their results to a friction coefficient of 0.6 raises their estimate of thermal anomaly to values consistent with most of the other studies. Zhang & Sagiya (2017) include both frictional and viscous shear heating in their model, in which earthquakes are kinematically imposed and the depth of the BDT is both gradual and determined self-consistently as part of the solution. They find that for a continental strike-slip fault, the overall thermal anomaly peaks at roughly 200 °C at about 12 km depth, which is sufficient to produce a shallower BDT than in an otherwise equivalent model without shear heating. Lambert & Barbot (2016b) also account for both frictional and viscous shear heating, modeling a fault with rate-and-state friction embedded in an elastic layer overlying a viscoelastic half-space. They find the magnitude of the overall thermal anomaly to be on the order of 100-200 °C, centered in the middle of the 15-km-deep velocity-weakening zone. Both Zhang & Sagiya (2017) and Lambert & Barbot (2016b) find that frictional shear heating is larger than viscous shear heat-

ing, a result which might differ if dynamic weakening were included in the coseismic period.

In this study, we develop and utilize a thermomechanical earthquake sequence model which simulates earthquake cycles with a rate-and-state frictional fault in viscoelastic half-space obeying a temperature-dependent power-law rheology. The mechanics problem is coupled to the heat equation with frictional and viscous shear heating source terms. Our primary focus is on representing the BDT zone as a broad region whose depth is not imposed a priori, but rather emerges from the solution of the governing equations and changes in response to variable stresses and shear heating. In order to focus on temperature-dependent effects, we consider a single frictional and compositional structure. We perform a parameter-space study exploring the influence of the ambient geotherm, parameterized by the lithosphere-asthenosphere boundary (LAB) depth; pore fluid pressure, parameterized with the Hubbert-Rubey fluid pressure ratio; and the width of the frictional shear zone. Shallower LAB depths correspond to warmer ambient geotherms, which decrease the effective viscosity, producing a shallower BDT. Elevating pore fluid pressure reduces the effective normal and shear stress on the fault, thereby decreasing frictional shear heating. The lower shear strength of the fault also reduces deviatoric stresses in the off-fault material, hence lowering viscous shear heating as well. Increasing the width of the frictional shear zone decreases the local temperature rise (within a few meters of the fault) produced by frictional shear heating, but otherwise results in minimal changes in the model behavior.

2 Model

We model a vertical strike-slip fault in a viscoelastic half-space undergoing two-dimensional antiplane shear deformation (Figure 1). The fault is located at $y = 0$, where y is horizontal and z is vertical and pointing down, with the origin located at the intersection of the fault with the Earth's surface. To reduce computational cost, we use material properties and tectonic loading that are symmetric about the fault, allowing us to model only half of the domain ($y \geq 0$). In this study, we use the quasi-dynamic approximation to elastodynamics (i.e., quasi-static deformation with the radiation damping approximation, Rice, 1993), but future efforts can account for full elastodynamics as we have demonstrated in another study that utilizes the same code (Duru et al., 2019). The fault exists through the entire model domain so that the depth of the BDT, and the partitioning of tectonic loading into fault slip and bulk viscous flow, can be determined by the depth-dependent relative strength of the fault and off-fault material, rather than being imposed a priori. Below we state the governing equations and boundary conditions.

The static equilibrium equation is

$$\frac{\partial \sigma_{xy}}{\partial y} + \frac{\partial \sigma_{xz}}{\partial z} = 0, \tag{1}$$

where σ_{ij} are the quasi-static stress components, which are given by Hooke's law,

$$\sigma_{xy} = \mu \left(\frac{\partial u}{\partial y} - \gamma^V_{xy} \right), \quad \sigma_{xz} = \mu \left(\frac{\partial u}{\partial z} - \gamma^V_{xz} \right), \tag{2}$$

where u is the displacement in the x direction, γ^V_{ij} are the (engineering) viscous strains, and μ is the shear modulus. The viscous strains are determined by the power-law viscous flow law

$$\dot{\gamma}^V_{xy} = \eta^{-1}_{\text{eff}} \sigma_{xy}, \quad \dot{\gamma}^V_{xz} = \eta^{-1}_{\text{eff}} \sigma_{xz}, \tag{3}$$

$$\eta^{-1}_{\text{eff}} = A e^{-Q/RT} \bar{\tau}^{n-1}, \quad \bar{\tau} = \sqrt{\sigma^2_{xy} + \sigma^2_{xz}}, \tag{4}$$

where the overdot indicates a time derivative, η_{eff} is the effective viscosity, T is the temperature, and R is the universal gas constant. The effective viscosity is a nonlinear func-

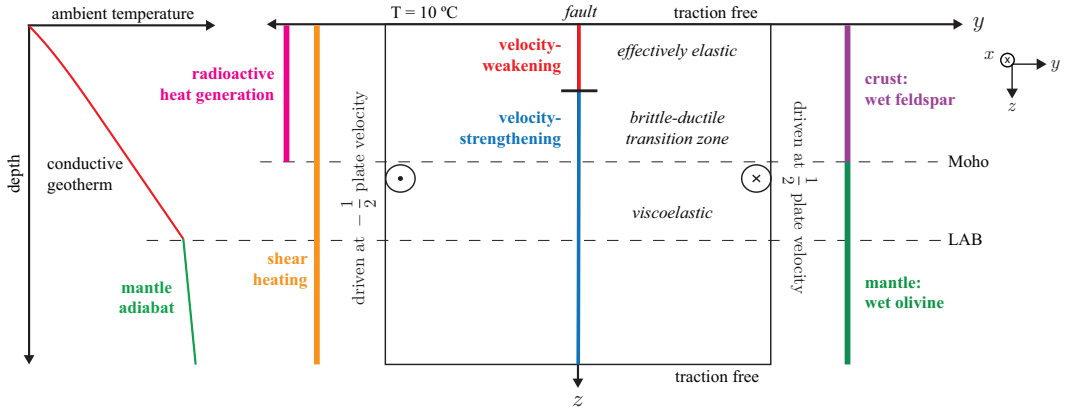

Figure 1. Our 2D strike-slip fault model simultaneously captures the transition from velocity-weakening (VW) to velocity-strengthening (VS) rate-and-state friction and the off-fault transition from effectively elastic to viscoelastic deformation. The depths of both transitions depend on temperature, so we consider a range of ambient geotherms, using a conductive geotherm in the crust and an adiabat below the lithosphere-asthenosphere boundary (LAB). We also account for thermal anomalies arising from frictional and viscous shear heating by simultaneously solving the heat equation.

tion of the deviatoric stress invariant $\bar{\tau}$, and also depends upon several rheological parameters which vary with composition: the rate coefficient A, the activation energy Q, and the stress exponent n. Deviatoric stresses and in-plane viscous flow are neglected.

On the fault, frictional strength (i.e., the shear resistance to sliding), τ, balances the resolved shear traction on the fault, accounting for the radiation-damping response (Rice, 1993):

$$\tau(z,t) = \sigma_{xy}(0,z,t) - \eta_{rad} V = f(\psi, V)\bar{\sigma}_n, \tag{5}$$

$$\dot{\psi} = G(\psi, V), \tag{6}$$

$$\delta(z,t) \equiv 2u(0,z,t), \tag{7}$$

$$V \equiv \frac{\partial \delta}{\partial t}. \tag{8}$$

where $\bar{\sigma}_n$ is effective normal stress, ψ is the state variable, V is slip velocity, δ is slip, and f is the friction coefficient. Equation (6) is the state evolution equation, e.g., either the slip law or the aging law (in this study we use the aging law).

Boundary conditions on the exterior sides of the domain are

$$\sigma_{xz}(y,0,t) = 0, \tag{9}$$

$$\sigma_{xz}(y,L_z,t) = 0, \tag{10}$$

$$u(L_y,z,t) = \frac{V_L t}{2} \tag{11}$$

where L_y and L_z are the dimensions of the model domain in the $y-$ and $z-$directions, respectively, and V_L is the tectonic plate (i.e., loading) velocity. At Earth's surface, we use a traction-free boundary condition (9). We also use this boundary condition at the bottom of the domain, because it permits an arbitrary amount of displacement to occur. This is necessary for elastic models, but is irrelevant in viscoelastic models, as viscous flow permits arbitrary displacements at the bottom of the domain as well. Tectonic loading displacement is applied at a steady rate to the lateral boundary. It is important

to use a sufficiently large domain such that the model behavior is independent of L_y or L_z (Erickson et al., 2020), so we place both boundaries at 500 km, or about 50 times the seismogenic depth, using a coordinate transform (i.e., grid stretching) for computational efficiency (Allison & Dunham, 2018).

We additionally solve the energy balance or heat equation for the perturbation ΔT, or thermal anomaly, from the ambient one-dimensional geotherm T_{amb}. Above the LAB, T_{amb} corresponds to steady-state vertical conduction with radiogenic heat generation in the crust, and below the LAB it follows the mantle adiabat (Turcotte & Schubert, 2002):

$$\frac{d}{dz}\left(k\frac{dT_{\text{amb}}}{dz}\right) + Q_{\text{rad}} = 0,\ 0 < z < z_{\text{LAB}}, \tag{12}$$

$$Q_{\text{rad}} = A_0 e^{-z/d_r}, \tag{13}$$

$$T_{\text{amb}}(y, 0, t) = T_0 \tag{14}$$

$$T_{\text{amb}}(z_{\text{LAB}}) = T_p + g z_{\text{LAB}}, T_{\text{amb}}(z) = T_p + gz,\ z \geq z_{\text{LAB}}, \tag{15}$$

where Q_{rad} is the source term for radiogenic heat generation in the crust, T_p is the mantle potential temperature, and g is the slope of the mantle adiabat. To solve for T_{amb} above the LAB, we hold the temperature at the Earth's surface fixed at $T_0 = 10°\text{C}$, and at z_{LAB} the temperature is determined by the mantle adiabat.

The heat equation for the thermal anomaly ΔT, which is solved over the entire domain (both above and below the LAB) is

$$\rho c\frac{\partial \Delta T}{\partial t} = \frac{\partial}{\partial y}\left(k\frac{\partial \Delta T}{\partial y}\right) + \frac{\partial}{\partial z}\left(k\frac{\partial \Delta T}{\partial z}\right) + Q_{\text{visc}} + Q_{\text{fric}}, \tag{16}$$

$$Q_{\text{visc}} = \bar{\tau}\dot{\bar{\gamma}}^V, \quad Q_{\text{fric}} = \frac{\tau V}{\sqrt{2\pi}w}\exp\left(\frac{-y^2}{2w^2}\right), \tag{17}$$

where ρ is the density, c is the specific heat, $\dot{\bar{\gamma}}^V = \sqrt{(\dot{\gamma}^V_{xy})^2 + (\dot{\gamma}^V_{xz})^2}$ is the second invariant of the viscous strain rate, and Q_{visc} and Q_{fric} are the source terms for viscous and frictional shear heating, respectively. We spread frictional shear heating over a Gaussian shear zone of half width w (e.g., Andrews, 2002; Rice, 2006), which we vary from 0.1 to 10 m. Geologic observations indicate that, in the shallow crust and for an individual earthquake, this frictional shear zone can be as narrow of tens of micrometers, suggesting that frictional shear heating could instead be included as a heat flux radiating from a planar fault (Rice, 2006). However, without the inclusion of a dynamic weakening mechanism such as thermal pressurization or flash heating, this would result in an unrealistically large coseismic temperature rise and the onset of melting (Rempel & Rice, 2006), which is neglected in our model. Our model can easily be extended to include dynamic weakening, but this would introduce additional free parameters and complexity, so we defer this important extension to future studies.

With regard to boundary conditions for ΔT, we hold the exterior boundaries fixed at the temperature of the ambient geotherm, and account for frictional heating only through a source term as described above:

$$\partial \Delta T/\partial y\big|_{y=0} = 0, \quad \Delta T(L_y, z, t) = 0, \quad \Delta T(y, 0, t) = 0, \quad \Delta T(y, L_z, t) = 0. \tag{18}$$

As in the mechanical problem, it is important that the domain is large enough that the thermal anomaly is not impacted by the remote boundary conditions. We use the same domain for both the heat equation and the mechanical problem, so this condition is easily satisfied.

The discretization of the governing equations is described in the Supporting Information. The grid spacing in the z-direction is chosen to resolve frictional dynamics. We also use a grid spacing of $w/5$ (0.02 m) in the y-direction near the fault to resolve thermal boundary layers that arise during the coseismic phase. Grid stretching is used away from the fault and seismogenic zone.

parameter	symbol	value
Frictional parameters		
direct effect parameter	a	depth variable, see Figure 3a
state evolution effect parameter	b	depth variable, see Figure 3a
state evolution distance	d_c	3.2, 6.3, 10 mm
reference friction coefficient for steady sliding	f_0	0.6
reference velocity	V_0	10^{-6} m/s
radiation damping coefficient	η_{rad}	4.68 MPa s/m
Hubbert-Rubey pore pressure ratio	λ	0.8, 0.6, 0.37
effective normal stress	$\bar{\sigma}_n$	depth variable, see Figure 3c
nucleation zone size	h^*	5 km at 12 km
Viscoelastic parameters		
shear modulus	μ	30 GPa
density	ρ	2700 kg/m^3
loading velocity	V_L	10^{-9} m/s
Moho depth	z_{Moho}	30 km
Thermal parameters		
surface radiogenic heat production rate per unit mass	A_0	2 μW/m^2
length scale for radiogenic heat generation	d_r	10 km
mantle adiabat	g	0.3°C/km
thermal conductivity	k	2.5 W/m/K
Earth's surface temperature	T_0	10 °C
mantle potential temperature	T_p	1200 °C
frictional shear zone width	w	0.1 - 10 m
LAB depth	z_{LAB}	40 - 70 km
thermal diffusivity	α_{th}	1 mm^2/s
heat capacity	ρc	2.5 MJ/°C m^3

Table 1. Model parameters. Note that state evolution distance d_c is varied with pore pressure ratio λ in order to keep nucleation length unchanged.

2.1 Ambient Geotherms

The power-law rheology is strongly temperature-dependent, and therefore the choice of ambient geotherm makes a significant difference in the behavior of the system. We consider four candidate geotherms (Figure 2), selected to be representative of southern California. The geotherms are consistent with observations of surface heat flow of 60-120 mW/m^2 (Lachenbruch et al., 1985; Williams & DeAngelo, 2011) and estimates of the Moho temperature of 650-850 °C (Humphreys & Hager, 1990; Yang & Forsyth, 2008). Exhumed xenoliths originating from a few kilometers below the Moho in the Mojave region are consistent with the upper end of this Moho temperature range (Behr & Hirth, 2014). The geotherms are constructed assuming a surface temperature of 10°C, a mantle adiabat of 0.3°C/km, and mantle potential temperature of 1200°C (Lachenbruch & Sass, 1977). Radiogenic heat generation is included only in the crust above the LAB, with the heat production decaying exponentially with depth, as defined in Equation (13) (Lachenbruch & Sass, 1977). Based on Lekic et al. (2011), we consider four LAB depths: 40, 50, 60, and 70 km. For simplicity, we assume constant thermal parameters throughout the domain, given in Table 1 (Turcotte & Schubert, 2002).

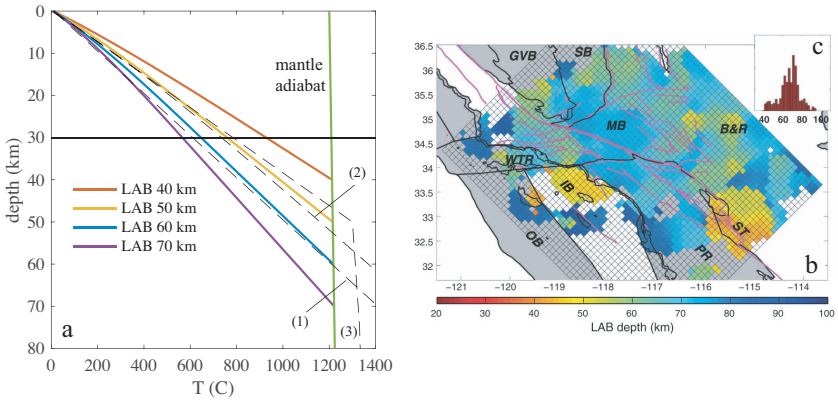

Figure 2. (a) Ambient geotherms constructed using a conductive geotherm in the lithosphere, including radiogenic heat generation in the crust, and a mantle adiabat, representative of a convective regime. The LAB is the depth at which the conductive geotherm intersects the mantle adiabat. We consider four LAB depths: 40, 50, 60, and 70 km. The dashed black lines show geotherms used in other, similar studies: (1) Takeuchi & Fialko (2012), (2) Sass et al. (1997), and (3) Freed & Bürgmann (2004) and Takeuchi & Fialko (2013). (b) and (c) LAB depths in southern California, reproduced from Lekic et al. (2011).

2.2 Rheological Parameters

We consider a single, layered composition, representing the crust with wet feldspar and the mantle with wet olivine. The transition in composition from the crust to the mantle occurs smoothly over 10 km, as shown in Figure 3b, using a mixing law representative of magmatic underplating, as in Allison & Dunham (2018). Also, we neglect spatial variation in the shear modulus, instead using the constant value given in Table 1. We assume the viscous deformation mechanisms to be dislocation creep in both the crust and mantle, though there is evidence that feldspar in the lower crust deforms through diffusion creep as well, particularly in shear zones where the grain size is reduced (Rybacki & Dresen, 2004). While our method can handle diffusion creep and different rheologies in shear zones, we defer this to future work (Allison & Montesi, 2020).

material	A (MPa^{-n} s^{-1})	n	Q (kJ mol^{-1})	source
wet feldspar	1.58×10^3	3	345	Rybacki et al. (2006)
wet olivine	3.6×10^5	3.5	480	Hirth & Kohlstedt (2003)

Table 2. Values used for power-law flow parameters.

2.3 Stress State

The frictional strength of the fault (5) is intimately related to the stress state of the system, which is essential to specify given the nonlinearity of the viscous flow law and rate-and-state friction law. We set the overall stress state, which enters our model solely through the effective normal stress on the fault in equation (5), by assuming an optimally oriented strike-slip fault having friction coefficient $f_0 = 0.6$ (e.g., Sibson, 1974). We assume vertical total stress is equal to lithostatic pressure, and consider different conditions for pore pressure at depth, parameterized with the Hubbert-Rubey fluid pressure ratio λ (equal to pore pressure divided by lithostatic pressure) (Hubbert & Rubey, 1959).

We first consider the case of hydrostatic pore pressure, $\lambda = 0.37$ for the rock density used in this study. We also consider two cases of elevated pore pressure: $\lambda = 0.6$ and 0.8. Note that this background stress state produces both antiplane and in-plane deviatoric stresses. As explained earlier, we neglect the contribution of in-plane deviatoric stresses in our application of the viscous flow law, such that the resulting deformation is exclusively 2D antiplane shear. This does limit the applicability of our results for certain applications, such as quantifying the orientation and relative magnitude of the principal stresses, which require fully 3D calculations.

2.4 Frictional Parameters

The frictional strength of the fault is governed by rate-and-state friction. We use the regularized form (Rice et al., 2001),

$$f(\psi, V) = a \sinh^{-1}\left(\frac{V}{2V_0} e^{\psi/a}\right) \approx a \ln\left(\frac{V}{V_0}\right) + \Psi, \tag{19}$$

with the aging law for state evolution (Ruina, 1983; Marone, 1998),

$$G(\psi, V) = \frac{bV_0}{d_c}\left(e^{(f_0-\psi)/b} - \frac{V}{V_0}\right). \tag{20}$$

This formulation can be brought into the more common form of rate-and-state friction by replacing our choice of (dimensionless) state variable, Ψ, with the usual state variable θ (having units of time) via $\Psi = f_0 + b\ln(V_0\theta/d_c)$, such that $f \approx f_0 + a\ln(V/V_0) + b\ln(V_0\theta/d_c)$ and $G = 1 - V\theta/d_c$. However, Ψ, as a nondimensional quantity of order unity, is better suited for numerical calculations. The primary parameters which determine the frictional behavior of the system are the direct effect parameter a, the state evolution parameter b, and the state evolution distance d_c. Velocity-weakening (VW) regions with $a-b < 0$ have the potential for unstable sliding, where velocity-strengthening (VS) regions with $a-b > 0$ generally slip aseismically unless forced by a dynamic rupture. Due to the increase in temperature with depth, friction transitions from VW to VS with increasing depth. This transition in frictional behavior may control the down-dip limit of ruptures; however, the experimental results of Mitchell et al. (2016), performed up to 600°C on granite, suggest that friction may remain VW to the depth of the BDT for most geotherms. In this case, the down-dip limit of ruptures would be determined by the BDT instead.

To set the depth dependence of a and b, we use laboratory data for wet granite gouge from Blanpied et al. (1991, 1995), reproduced in Figure 3a. The wet granite data have been used extensively in earthquake cycle simulations (e.g., Rice, 1993; Lapusta et al., 2000; Lapusta & Rice, 2003b; Kato, 2002; Lindsey & Fialko, 2016; Allison & Dunham, 2018). The data predict a shallow transition from VS to VW at about 100°C and a deeper transition back to VS at around 350°C; however, as our focus is on the behavior of the system at depth, we neglect the shallow transition. To assign depth dependence of frictional properties from temperature-dependent data, we use the ambient geotherm for a 60 km deep LAB. For simplicity, we use the same depth distribution of frictional properties for all simulations. We also neglect changes in frictional parameters as a result of the changes in temperature produced by shear heating. Since the fault exists through the entire depth of the model, we use linear extrapolation to assign values below the last data point, based on the theoretically expected linear dependence of a on temperature (Rice et al., 2001). For d_c, laboratory data indicates that it is on the order of a few to tens of microns (e.g., Dieterich, 1979; Marone & Kilgore, 1993); however, to reduce the computational expense, we use $d_c = 10$ mm in the model with hydrostatic pore pressure. This corresponds to a 5 km nucleation zone, estimated as $h^* = \mu d_c/(\bar{\sigma}_n(b-a))$, at 12 km depth (the approximate depth of nucleation in elastic models with these parameters). We change d_c to keep h^* constant at this depth in models with elevated pore pressure. More details are provided in Supporting Information.

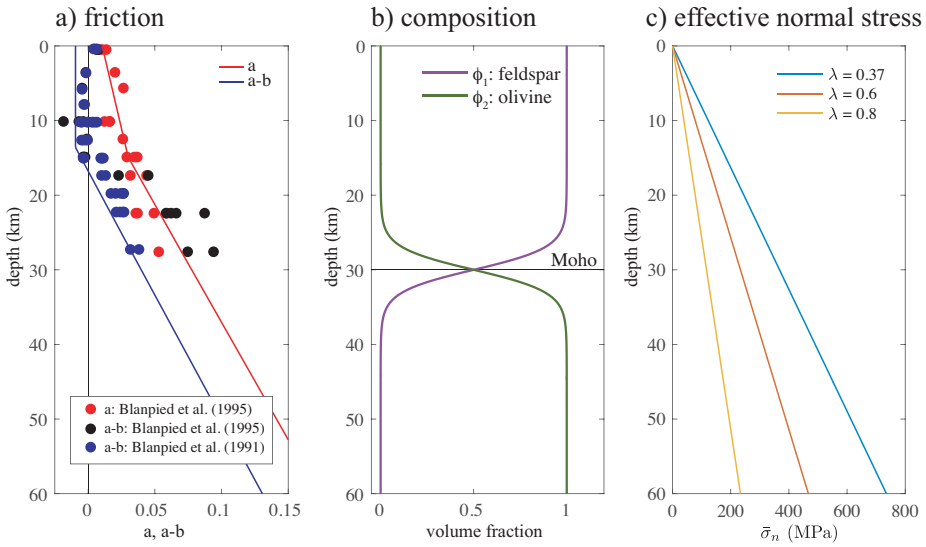

Figure 3. (a) Rate-and-state laboratory data for a and a-b for wet granite from Blanpied et al. (1991, 1995) shown as dots, and model parameters shown as solid lines. The data have been converted from temperature to depth using a the geotherm for a 60 km deep LAB. (b) Volume fractions for feldspar and olivine, smoothly transitioning across the Moho depth of 30 km. (c) Effective normal stress for varying pore pressure: $\lambda = 0.37$ (hydrostatic pore pressure), 0.6, and 0.8.

3 Results

We first illustrate the effects of shear heating and viscous flow on the earthquake cycle by presenting results from a representative viscoelastic earthquake cycle simulation with shear heating. Results from this simulation are compared with those from an

otherwise identical viscoelastic simulation with no shear heating, in which temperature is fixed to the ambient geotherm, and an elastic simulation. Then, we present results from our steady-state simulations, which characterize many features of the system, such as the depth of the BDT and the stress distribution through the lithosphere. We also discuss the relative contributions of frictional and viscous shear heating, showing that both are of roughly equal magnitude. Finally, we summarize results of a parameter-space study varying the ambient geotherm (i.e., LAB depth), pore fluid pressure ratio λ, and frictional shear zone width, exploring how these parameters control characteristics of the earthquake cycle and the BDT depth.

3.1 Representative Viscoelastic Cycle Simulation with Shear Heating

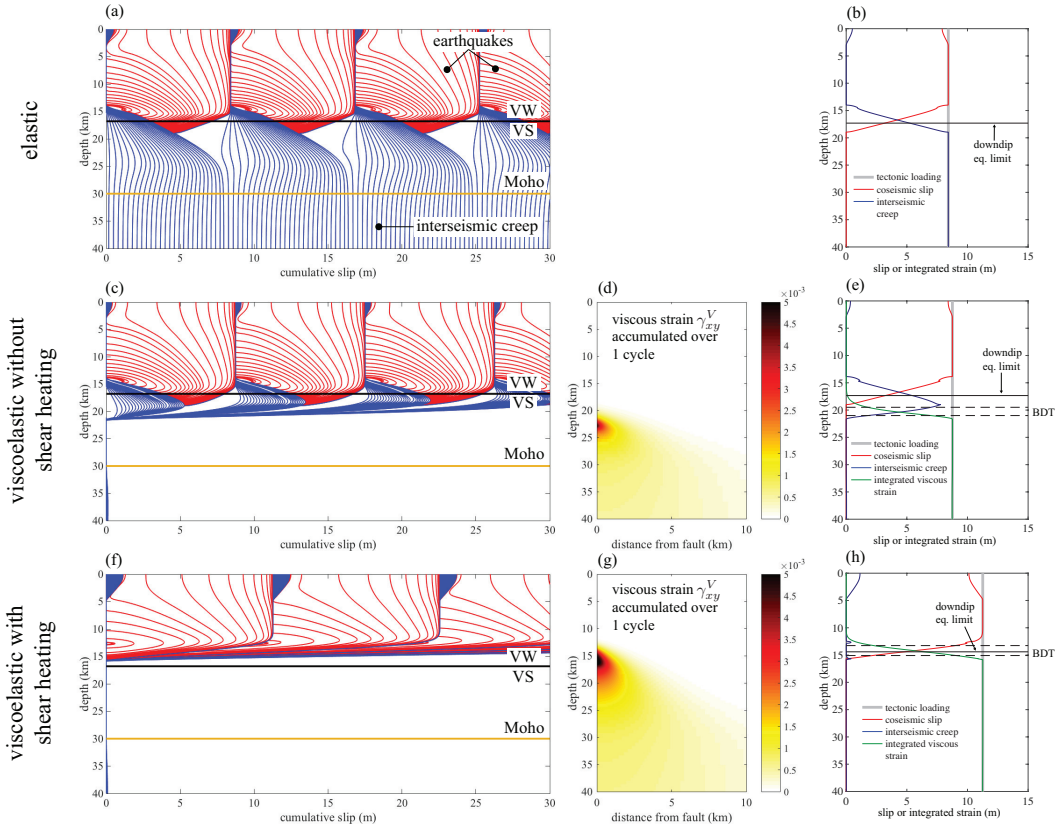

Figure 4. Comparison between elastic (top row), viscoelastic without shear heating (middle row), and viscoelastic with shear heating (bottom row) cycle simulations for a 50 km deep LAB, hydrostatic pore pressure, and $w = 1$ m. (a), (c), and (f) Cumulative slip, plotted in red every 1 s for coseismic slip and in blue every 10 years during the interseismic period. Shear heating shallows the earthquake cycle and the BDT. (d) and (g) Viscous strain γ^V_{xy} accumulated over one earthquake cycle. (b), (e), and (h) Partitioning of tectonic loading (grey) into coseismic slip (red), interseismic slip (blue), and bulk viscous flow (green, obtained by integrating γ^V_{xy} over horizontal lines at fixed depth). Also shown are the down-dip limit of the earthquake (black, solid) and depth of the BDT (black, dashed).

In this section, we summarize the results from a representative viscoelastic cycle simulation with shear heating with a 50 km deep LAB, hydrostatic pore pressure ($\lambda = 0.37$), and a $w = 1$ m wide frictional shear zone. Figure 4 compares the viscoelastic cy-

cle simulation with shear heating with equivalent viscoelastic without shear heating and elastic simulations; additional details are given in Supporting Information (specifically, Figure S1). In the elastic simulation (Figures 4a and b) the depths of earthquake nucleation and down-dip propagation are determined by the VW-VS transition. Deeper in the crust, tectonic loading is accommodated by frictional afterslip and interseismic fault creep. The depths of earthquake nucleation and down-dip propagation are the same in the viscoelastic simulation without shear heating (Figures 4c-e), and in fact the transition between coseismic and interseismic slip in the mid-crust is also very similar to that of the elastic simulation. This echoes results of our previous study (Allison & Dunham, 2018). In contrast, in the viscoelastic cycle simulation with shear heating (Figures 4f-h), coseismic slip is confined to shallower depths, because it is limited not by the transition in frictional properties but by the BDT.

In both viscoelastic simulations, tectonic loading in the lower crust is accommodated by off-fault viscous flow (Figures 4d and g). Viscous flow is concentrated near the fault at the depth at which fault slip ceases, and becomes more broadly distributed with depth. Shear heating produces only a slightly more localized shear zone, at least for the chosen parameters and rheology.

Comparing the cumulative slip plot for the viscoelastic cycle simulation with shear heating (Figure 4f), with that for the viscoelastic cycle simulation without shear heating (Figure 4c), it is evident that shear heating shallows the depth of earthquake nucleation and the down-dip limit of coseismic slip. However, the total coseismic slip per event is larger because the recurrence interval is larger.

Since these simulations are in a limit cycle, producing the same earthquake cycle periodically, the elastic strain in the system returns to the same level after each cycle (Savage & Prescott, 1978). Therefore, the tectonic loading displacement over one cycle is partitioned into coseismic and interseismic fault slip, and viscous flow:

$$\delta_{\text{co}} + \delta_{\text{int}} + \int_{-L_y}^{Ly} \gamma_{xy}^{V} dy = V_L T_{\text{rec}} \tag{21}$$

where δ_{co} is the coseismic slip, δ_{int} is the interseismic slip, and T_{rec} is the recurrence interval. Figures 4b, e, and h show the depth dependence of this partitioning. The solid black line shows a measure of the down-dip limit of coseismic slip, defined as the depth above which 98% of the total potency of the earthquake occurs. The dashed black lines show a measure of the depth of the BDT zone, defined as the depths between which 20% and 80% of the tectonic loading is accommodated by bulk viscous flow. In this case, the inclusion of shear heating shallows the BDT by about 5 km, causing it to overlap with the down-dip limit of coseismic slip, producing a 1.2-km-wide region in which one might find geologic evidence of both brittle and ductile deformation. This is discussed in greater detail in Section 3.3.

Figure 5 shows the thermal anomaly from shear heating, ΔT. The thermal anomaly from frictional shear heating during the coseismic phase persists into the early postseismic period, lasting for about 1 month (Figure 5a-d). It is initially concentrated over distance w from the center of the fault zone, then diffuses outward. Though the thermal anomaly produced by each earthquake is short-lived, a nonzero thermal anomaly persists through the interseismic period (Figure 5e); this is the cumulative effect of a long sequence of past earthquakes. Decreasing w causes the maximum transient thermal anomaly to increase (Figure 5f), but we find that it is so short-lived and localized that w has negligible impact on characteristics of the earthquake cycle, such as the recurrence interval, earthquake nucleation depth and down-dip limit, and BDT depth. For example, for the simulation with a 50 km LAB, $\lambda = 0.37$, and $w = 0.3$ m, the transient effect of shear heating is to drop the effective viscosity in the mid-crust (10-15 km depth) within 0.5 m of the fault to about 3×10^{13} Pa s, which corresponds to a Maxwell time of 1000 s. This causes viscous strain to accumulate in this region over the period of 1 day, corre-

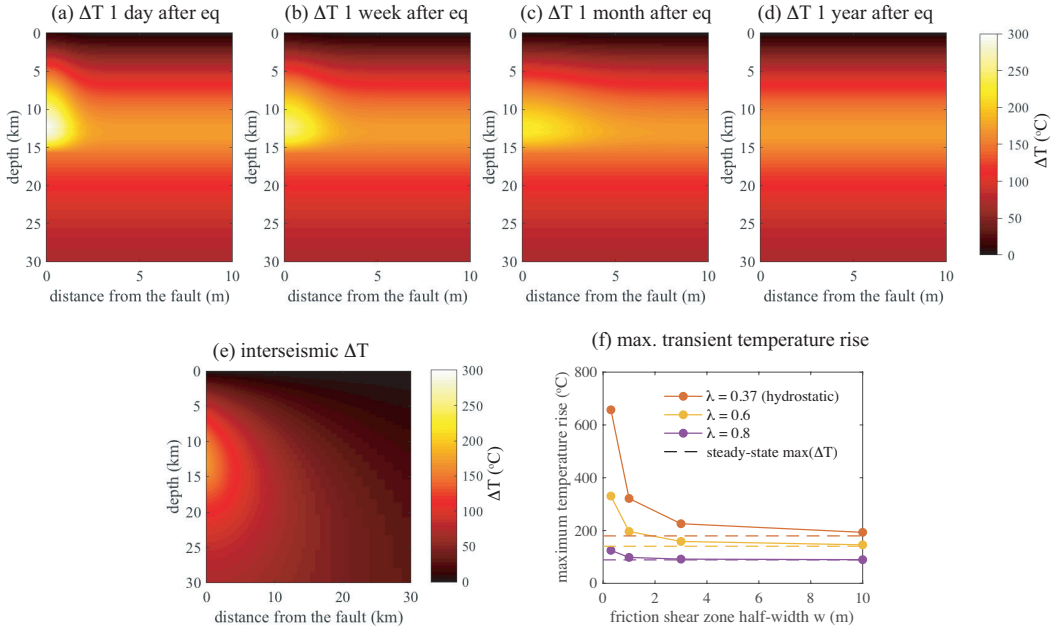

Figure 5. Evolution of thermal anomaly for the viscoelastic cycle simulation with shear heating with a 50 km deep LAB, hydrostatic pore pressure, and $w = 1$ m. (a)-(d) Snapshots of the thermal anomaly within one year after the earthquake, showing that the thermal anomaly from frictional heat generation lasts for a very short period of time, relative to the recurrence interval, and is restricted to the middle crust between 10 and 15 km depth. (e) Corresponding average interseismic thermal anomaly. Note the change in x-axis from (a)-(d) to (e). (f) Maximum transient thermal anomaly increases as the frictional shear zone half-width w shrinks, with the maximum of the thermal anomaly from the steady-state model plotted (dashed) for reference.

sponding to an additional offset across the fault of 1.3 mm (only 0.025% of the total tectonic offset over the cycle). Simulations with larger w produce smaller transient temperature rises.

3.2 Insight from Steady-State Results

In addition to viscoelastic cycle simulations with shear heating that resolve the transient slip dynamics (i.e., coseismic, postseismic, and interseismic phases), we also performed steady-state simulations in which fault slip velocity and off-fault viscous strain rates are constant in time (see Appendix A for details on the solution method). While this steady-state model is an approximation that neglects transient slip behavior like earthquakes, we find that it provides remarkably accurate predictions of the general lithospheric stress distribution, thermal anomaly, and heat flux. Therefore, in this section we use the steady-state model to explore the relative contributions of frictional and viscous shear heating to the thermal anomaly, and the effect of shear heating on the depth of the BDT. The frictional shear zone half-width w has no impact on these results within the range of w considered, because w is much smaller than the characteristic length scales of the heat generation region.

Shear heating significantly weakens the root of the fault and shallows the BDT, as illustrated in Figure 6. Weakening in the lower crust is greatest for simulations with low pore pressure and the coolest background geotherm. The case with an LAB depth of 50 km and hydrostatic pore pressure is explored in more detail in Figure 7a. The total ther-

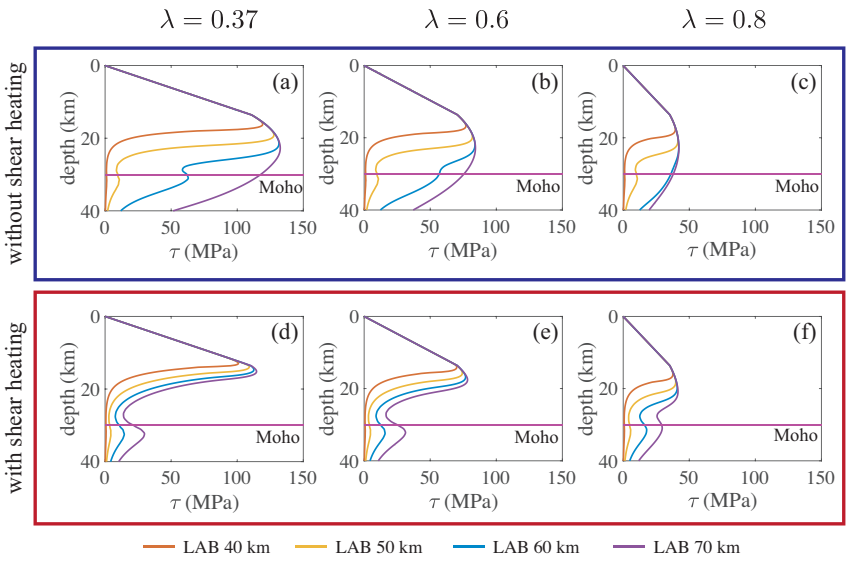

Figure 6. Shear stress on the fault and its deep extension for viscoelastic simulations with (right) and without (left) shear heating, with pore pressure increasing down the rows.

mal anomaly ΔT is shown in Figure 7d, and the portions of that anomaly produced by frictional and viscous shear heating (ΔT_{fric} and ΔT_{visc}, respectively) are plotted in Figure 7e and f. This division is obtained by linearity of the heat equation, with ΔT_{fric} and ΔT_{visc} computed a posteriori from a simulation that includes both contributions. Both contributions to the total thermal anomaly are of roughly similar magnitude, though they differ in spatial distribution. Frictional shear heating is most significant in the middle of the crust where the shear stress and slip velocity are both high. In contrast, ΔT_{visc} is concentrated at significantly greater depths because it is generated primarily at the depth of the BDT, where the viscous strain rate is highest. It also occurs over a broader spatial scale than frictional shear heating. Neglecting either frictional or viscous shear heating, resulting in the red and yellow curves in Figure 7a and the thermal anomaly plotted in Figure 7b and c, produces a smaller total thermal anomaly and therefore a deeper BDT. While the spatial distribution of the thermal anomalies produced by each source of shear heating are quite different, the shear stress profiles are relatively similar to each other, and quite different from the model which accounts for both sources. The effect of varying pore pressure on ΔT_{fric} and ΔT_{visc} is illustrated in the Supporting Information (Figure S2). Increasing pore pressure decreases ΔT, ΔT_{fric}, and ΔT_{visc}; however, ΔT_{fric} decreases less rapidly than ΔT_{visc}, and therefore constitutes a larger fraction of the total thermal anomaly for high pore pressures.

3.3 Parameter Space Study

In this section, we return to the results of our cycle simulations, summarizing the effects of shear heating on the depth of earthquake nucleation, the down-dip limit of coseismic slip, and the BDT. Additional results concerning thermal energy are shown in the Supporting Information (Figure S3). We also include steady-state results for comparison when appropriate. Figure 8 compares results for viscoelastic simulations with and without shear heating, as a function of LAB depth and λ. Frictional shear zone width w does not change any of these characteristics, and is held fixed at $w = 1$ m in the re-

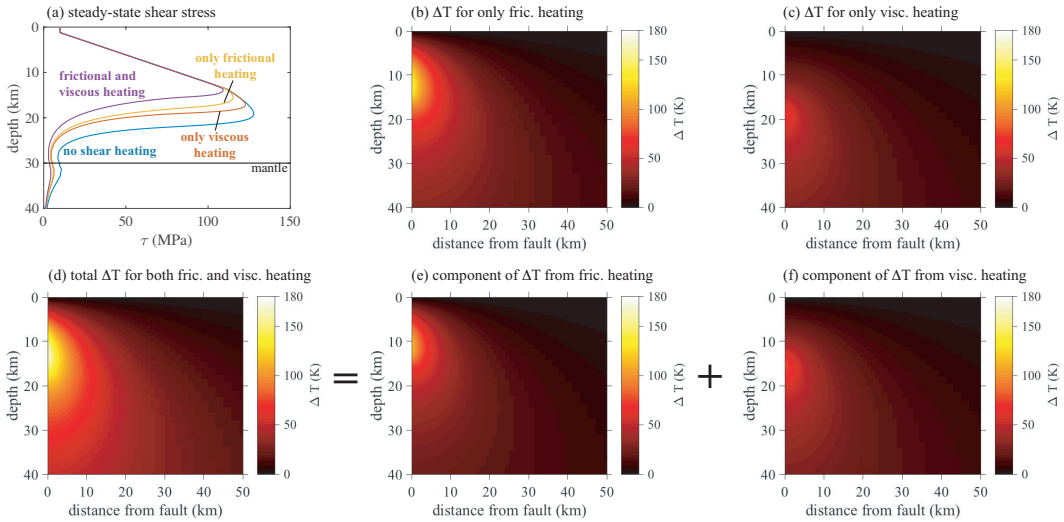

Figure 7. Results from steady-state model with an LAB at 50 km and hydrostatic pore pressure (all considered values of w produce these same results): (a) Shear stress on fault and its deep extension. (b)-(f) Thermal anomaly. (b) and (c) Thermal anomaly for simulations which include only frictional or viscous shear heating, respectively. (d) Total thermal anomaly for a simulation with both contributions to shear heating, and the portions of that anomaly which result from frictional and viscous shear heating are shown separately in (e) and (f). Frictional and viscous shear heating contribute relatively equally to the total thermal anomaly, and neglecting either one produces a much deeper BDT.

sults to follow. The nucleation depth is the depth at which the slip velocity first reaches coseismic levels, defined as 1 mm/s, consistent with the cumulative slip plots. We calculate the BDT from the cycle simulation results as described in Section 3.1, and also calculate the BDT depth range from the steady-state results, using the same definition. We also ran cycle simulations in which the transient effects of the cycles on the thermal anomaly were neglected, in which we used a time-independent temperature distribution taken from a corresponding steady-state simulation (thus accounting for the thermal anomaly but not its time evolution over the cycle). These simulations produced such similar results to the results with transient shear heating that they are not plotted here.

Turning now to our results, the BDT is much shallower for all viscoelastic simulations with shear heating than for corresponding simulations without shear heating. The viscoelastic simulations with shear heating all predict a BDT in the middle to lower crust, while many of the viscoelastic simulations without shear heating predict a BDT near or below the Moho. Additionally, for simulations with and without shear heating, the BDT becomes shallower for warmer geotherms (shallower LAB depths) and for decreasing pore pressure. Warmer geotherms lead to lower effective viscosity, and therefore a shallower BDT. Decreasing pore pressure leads to higher effective normal and shear stress on the fault, more heat generated by frictional shear heating, and thus a shallower BDT. The steady-state approximation for the BDT is quite accurate for most models, though it does predict a slightly deeper BDT for some of the viscoelastic simulations without shear heating with elevated pore pressure.

The depths of earthquake nucleation and down-dip propagation can be controlled by either the VW-VS transition on the fault, or the BDT. In the elastic simulations, there is no BDT, and therefore the VW-VS transition determines both depths. The viscoelastic simulations without shear heating produce very similar earthquake nucleation and

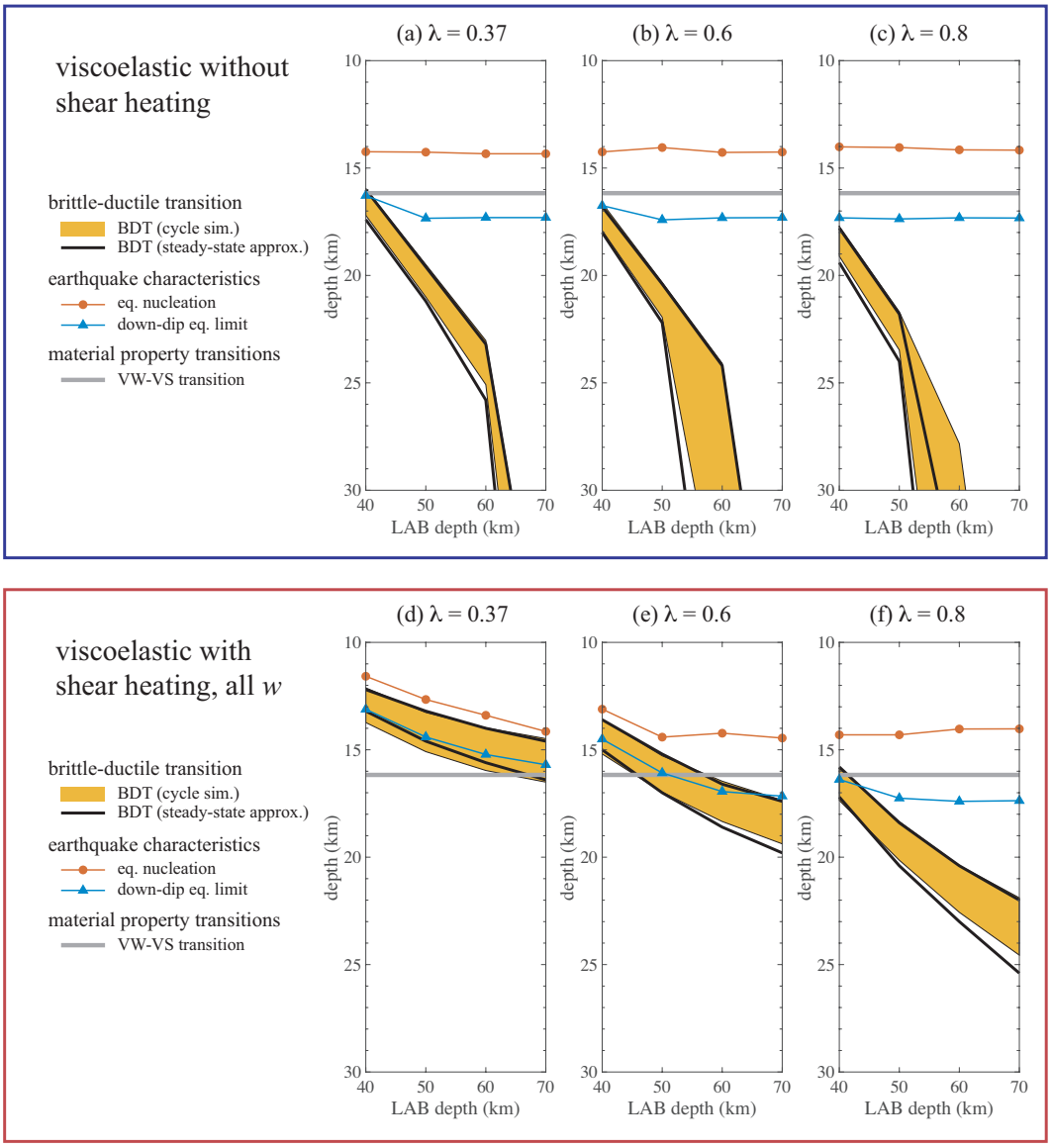

Figure 8. Comparison between earthquake nucleation depth (red circles), down-dip slip limit (blue triangles), and BDT depth range (yellow filled regions) for viscoelastic cycle simulations without (top row) and with (bottom row) shear heating. Also shown are estimates of the BDT from steady-state results (black lines).

down-dip propagation depths to the elastic simulations, indicating that these depths are also controlled by the VW-VS transition. In contrast, in the viscoelastic simulations with shear heating the down-dip coseismic slip limit is sometimes determined by the BDT rather than the VW-VS transition. For the parameters we consider, earthquakes never propagate all the way through the BDT. Therefore, when the BDT in the viscoelastic simulations with shear heating occurs above the down-dip coseismic slip limit in the elastic simulations, coseismic slip is limited to shallower depths. The same applies to earthquake nucleation, which always occurs above the BDT. Thus, viscoelastic simulations with shear heating with higher λ and shallower LAB depths have shallower BDTs, and as a consequence shallower earthquakes.

We also find that the recurrence interval of the viscoelastic simulations with and without shear heating sometimes differs from that of the equivalent elastic simulations. For the viscoelastic simulations without shear heating, slow slip events occur between the large earthquakes in some parts of parameter space (slow slip events do not occur in the elastic simulations), and in these cases the recurrence interval is increased by as much as 20 years. For viscoelastic simulations with shear heating, the recurrence interval changes by tens to hundreds of years, with the largest changes occurring for low λ where ΔT is largest; however, for some parameter choices, the recurrence interval is decreased while for others it is increased. For example, in Figure 4c, the recurrence interval is about 100 years longer. We speculate that this effect is caused by a change in the way remote loading is translated into loading of the seismogenic zone by deep viscous flow and/or aseismic slip. Alternatively, changes in the effective seismogenic zone extent, relative to the earthquake nucleation length, can influence recurrence interval dynamics by the introduction or suppression of smaller ruptures (Cattania, 2019).

These results show that the inclusion of viscoelastic deformation can impact the behavior of the seismogenic zone, such as nucleation depth and down-dip slip limit of coseismic slip, but only when the BDT is shallow enough that appreciable viscous flow occurs above the VW-VS transition. This explains why previous work on rate-and-state cycle simulations in viscoelastic solids by Kato (2002) and Allison & Dunham (2018) found that characteristics of the behavior of the seismogenic zone were not impacted by the inclusion of viscoelastic deformation at depth. The geometry of an elastic layer over a viscoelastic half-space used in Kato (2002) did not allow any overlap between the seismogenic zone, which was confined within the elastic layer, and the deeper viscoelastic half-space. And the simulations in Allison & Dunham (2018) were in a part of parameter space in which the BDT was much deeper than the seismogenic zone because shear heating was not included, as in the viscoelastic simulations without shear heating shown in this study.

The temperatures which correspond with the depths plotted in Figure 8 are shown in Supporting Information (Figure S4). The steady-state approximation for the BDT is again quite accurate. Additionally, the viscoelastic simulations with shear heating consistently place the BDT at about 550–600°C. This is the temperature range in which, for strain rates between 10^{-14}–10^{-12} s^{-1}, the viscous strength of feldspar becomes weaker than the frictional strength of the fault, shown in Figure 9. The viscoelastic simulations without shear heating place in the BDT in the same 550–600°C range when it occurs within the crust. These simulations place the BDT at a much higher temperature when it occurs in the mantle because olvine has a larger dislocation creep activation energy than feldspar, and a correspondingly higher BDT temperature.

3.4 Surface Heat Flux

Our model makes predictions of surface heat flux q, permitting comparison to measurements. In Figure 10, we compare our steady-state surface heat flux predictions with measurements for the creeping section of the San Andreas, near Parkfield (Fulton et al., 2004). As expected, the magnitude of the predicted anomaly in q near the fault is smaller for cooler ambient geotherms and elevated pore pressures. The ambient geotherm in this region is best represented by our geotherms for LAB depths of 50 and 60 km (Sass et al., 1997). There is a large amount of scatter in the data; however, it is clear that of the simulations with both frictional and viscous shear heating considered here, only those with substantially elevated fluid pressure ($\lambda = 0.8$) can be considered consistent with the data.

Elevated pore pressure has been suggested as a solution to the stress-heat flow paradox before (e.g., Byerlee, 1990; Rice, 1992; Tembe et al., 2009; Fulton & Saffer, 2009). A number of alternative solutions for the paradox have also been proposed, however. In

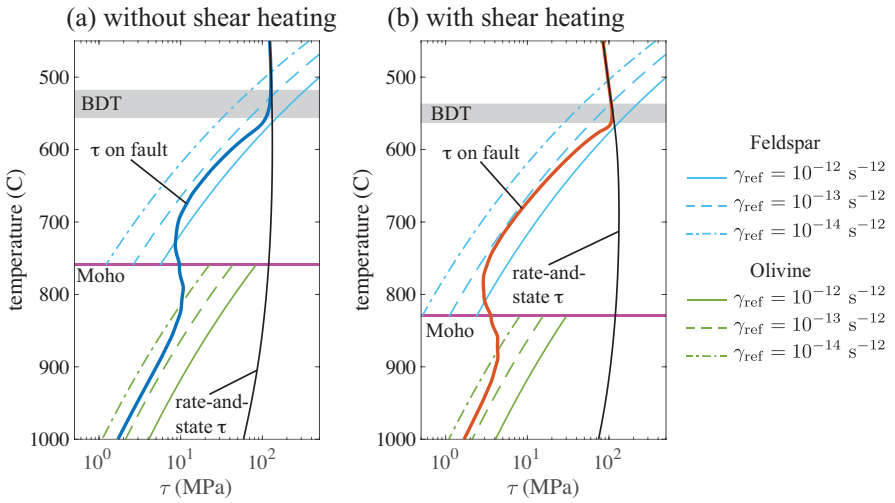

Figure 9. Comparison between shear stress on fault and predicted shear stress assuming a constant reference strain rate, for simulations with a 50 km deep LAB and hydrostatic pore pressure.

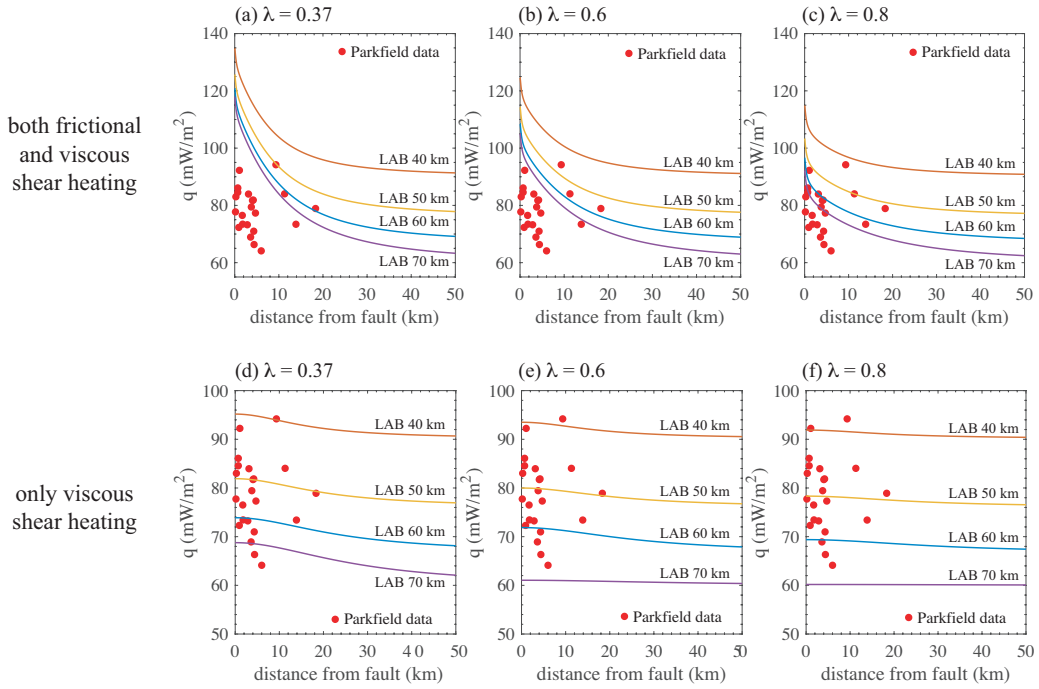

Figure 10. Comparison between surface heat flux simulation results (lines) and data (red points). (a) - (c) show results from simulations with both frictional and viscous shear heating. (d) - (f) show results from simulations with only viscous shear heating. Red points are measurements of heat flux as a function of distance from the San Andreas Fault, from Fulton et al. (2004). For the simulation results, the ambient geotherm determines the background heat flux far from the fault. Elevated pore pressure significantly reduces the magnitude of the anomaly near the fault.

particular, dynamic weakening reduces coseismic frictional heat generation, and can reduce the cycle-averaged thermal anomaly from frictional shear heating by allowing faults to operate at lower background stress levels (Lapusta & Rice, 2003a). Our simulations suggest that a weaker fault will also lead to smaller stresses in the off-fault material, and to a smaller thermal anomaly from viscous shear heating as well. As a rough proxy for the effect of dynamic weakening on frictional shear heating, neglecting its effects on the long-term strength of the fault, we also consider simulations in which only viscous shear heating is included, and frictional shear heating is neglected, in the bottom row of Figure 10. Because the thermal anomaly from viscous shear heating is relatively deep, the magnitude of the peak in surface heat flux near the fault is smaller than the scatter in the data. This suggests that, for simulations which do not produce clearly excessive heat flux near the fault, whether through the inclusion of elevated pore pressure, dynamic weakening, or another mechanism, it would be quite difficult to differentiate between models with surface heat flux data alone.

4 Discussion

4.1 Magnitude and Significance of Shear Heating

In this study, we quantified the effects of both frictional and viscous shear heating. Frictional shear heating produces transient changes in temperature in the mid-crust in the coseismic and postseismic period, which for small shear zone widths w can reach hundreds of degrees Celsius. But most results are insensitive to these temperature changes, as a result of the short lifespan and limited spatial extent of the transient temperature rise. Additionally, features like the interseismic thermal anomaly and the depth of the BDT are well-characterized by a steady-state approximation, in which the effects of earthquake cycles are approximated with time-independent slip velocity and viscous strain rates. Furthermore, cycle simulations which use the steady-state thermal anomaly and neglect transient shear heating effects all together produce very similar system behavior to those which include the transient effects, at a significant reduction in computational cost. These results demonstrate that viscous flow of the transiently thermally weakened region immediately around the fault is unlikely to contribute to early postseismic deformation, or be misinterpreted as afterslip.

We find that the steady-state thermal anomaly peaks in the mid-crust at 70–200 °C, with contributions from both frictional and viscous shear heating. Our findings for the magnitude and spatial distribution of the total thermal anomaly results are broadly consistent with those of Lambert & Barbot (2016a) and Zhang & Sagiya (2017), who found that the total thermal anomaly peaks in the middle of the seismogenic zone at 120 °C and 219 °C, respectively. Previous work which included only viscous shear heating predict widely differing magnitudes of the expected thermal anomaly, with some predicting an anomaly on the order of 1–10 °C (Lyzenga et al., 1991; Savage & Lachenbruch, 2003), essentially negligible, and others predicting an anomaly in the range of 150–200 °C (Thatcher & England, 1998; Leloup et al., 1999; Takeuchi & Fialko, 2012; Moore & Parsons, 2015). Our results are most consistent with the latter models. We attribute the differences with Lyzenga et al. (1991) to their use of a much weaker viscous flow rheology that placed the BDT around 7 km depth, shallower than in our model, and much smaller (by about a factor of 20) heat production at a given stress level. Savage & Lachenbruch (2003) utilized a much smaller friction coefficient, which if set to 0.6 would produce a comparable thermal anomaly to ours.

Comparison with observations of surface heat flux is one test of the results presented here. We find that, for the simulations considered, substantially weakened faults (in our simulations, weakening results from elevated pore pressure) are necessary for the predicted surface heat flux to be comparable with data from the Parkfield region of the San Andreas. This result could be impacted by a number of additional mechanisms and model

parameter choices. Regional variations in composition, degree of magmatic underplating, the passage of the triple junction and slab window, and the opening of a nearby rift like in Salton Trough, might lead to differences from our model predictions (e.g., Fulton & Saffer, 2009; Liu et al., 2012; Han et al., 2016; Neumann et al., 2017; Thatcher & Chapman, 2018). Additionally, dynamic weakening can reduce the background stress in the seismogenic zone, reducing the heat generated by frictional shear heating and therefore reducing the thermal anomaly and predicted surface heat flux. Our models suggest that a weaker seismogenic zone would also produce lower stresses in the off-fault material, decreasing the heat generated by viscous shear heating as well. It would be straightforward to investigate the effects of dynamic weakening by changing the form of rate-and-state friction used here to include flash heating or by extending the model to include thermal pressurization (Rice, 2006; Noda et al., 2009; Noda & Lapusta, 2010).

Our predictions for the thermal anomaly might ideally be compared with geologic indicators of viscous shear heating in exhumed shear zones. Arguably the most compelling of these comes from granulite and eclogite facies rocks of the North Davenport shear zone, a strike-slip system in dry, strong, continental crust in the Musgrave Block, Australia. Camacho et al. (2001) infer a thermal anomaly of ~ 200 °C (in eclogite facies at approximately 1.2 GPa pressure) in the shear zone relative to the country rock 1 km away. The thermal anomaly is inferred by radiometric dating from differences in closure ages during exhumation (with the initially hotter shear zone having a younger closure age than the country rock) and a heat conduction model to describe cooling during exhumation. This thermal anomaly is larger than predicted by our models at the relevant depths near the LAB. We note, however, that they attribute the thermal anomaly to viscous shear heating acting over a relatively short time, 0.03 – 0.3 Ma, which is too short for the steady-state assumptions made in this paper to apply.

Shear heating has also been suggested as an explanation for inverted metamorphic sequences around faults (England, 1993). Specifically, some have attributed higher-grade metamorphism within fault zones to the thermal anomaly from viscous shear heating (Leloup & Kienast, 1993; Leloup et al., 2001). However, it is unclear if shear heating is sufficiently large to explain the metamorphism (Gilley et al., 2003), and some alternative geologic interpretations suggest that metamorphism preceded the onset of shearing (Searle et al., 2010). This subject remains quite controversial (Leloup et al., 2007; Kidder et al., 2013).

4.2 Fault and Ductile Shear Zone Structure

Our results are broadly consistent with observations of the structure of strike-slip faults and their ductile roots. However, several assumptions are required to connect our simulations to geological structures like mylonite zones. Mylonites are characterized by reduced grain size and shear deformation fabrics, produced by dynamic recrystallization during viscous flow (Warren & Hirth, 2006; Platt & Behr, 2011). Our simulations predict viscous flow, but it is an ongoing effort to add grain size evolution (and grain-size sensitive flow laws like diffusion creep) to earthquake sequence simulations (Allison & Montesi, 2020). For this discussion, we assume a correspondence between viscous flow and mylonite structures. All of our simulations predict a shear zone that is a few kilometers wide in the lower crust, which is comparable to the width of the exhumed mylonite zone from the middle and lower crust beneath the Alpine Fault (Norris & Cooper, 2003; Norris & Toy, 2014) and the Salzach–Ennstal–Mariazell–Puchberg Fault (Rosenberg & Schneider, 2008). This is much narrower than the tens of kilometers spanned by major exhumed mylonite zones (Bell, 1978; Berthe et al., 1979; Weijermars, 1987; Camacho et al., 1995; Hanmer, 1988), supporting the hypothesis that these shear zones developed beneath a complex of multiple faults (Norris & Cooper, 2003).

Our simulations explore the relationship between the down-dip limit of coseismic slip in seismogenic earthquakes and the depth of the BDT. Our viscoelastic simulations

without shear heating, with the exception of those with a 40 km deep LAB (which is shallower than observed in much of southern California (Lekic et al., 2011)), predict a very deep BDT, such that there is no overlap between coseismic slip and appreciable viscous flow. This is consistent with our findings in Allison & Dunham (2018) (which use a less mafic composition for the crust), and matches the structure (elastic layer containing a fault over a viscoelastic half-space) assumed in related studies (Kato, 2002; Lambert & Barbot, 2016a). In contrast, all of our viscoelastic simulations with shear heating predict a shallow BDT in the mid-crust, and those with $\lambda < 0.8$ predict a zone in the mid-crust in which coseismic slip and viscous flow both occur. Thus, we find our viscoelastic simulations with shear heating are consistent with observations of faults which root in shear zones in the lower crust (Klosko et al., 1999; Molnar, 1999; Weber et al., 2004; Wilson et al., 2004), and many are consistent with observations of zones in which both viscous flow and coseismic slip occur (Vissers et al., 1997; Sibson & Toy, 2006; Lin et al., 2005; Cole et al., 2007; Griffith et al., 2008; Frost et al., 2011; White, 2012; Kirkpatrick & Rowe, 2013).

In all our simulations, we held the frictional transition from VW-VS fixed at 16 km depth regardless of the background geotherm and thermal anomaly. If instead the VW-VS transition was held at 350 °C and allowed to vary in depth and time, the nucleation depth and down-dip limit of earthquakes might be controlled by the VW-VS transition rather than the BDT for all simulations. On the other hand, recent experimental data shows that Westerly granite can remain VW up to at least 600 °C (Mitchell et al., 2016). In this case, the BDT would serve as the limit for both earthquake nucleation and down-dip coseismic slip.

For some faults, such as the San Jacinto, the Newport-Inglewood, and parts of the San Andreas, deformation remains highly localized all the way to the Moho (Lemiszki & Brown, 1988; Henstock et al., 1997; Zhu, 2000; Vauchez & Tommasi, 2003; Lekic et al., 2011; Miller et al., 2014; Inbal et al., 2016). This might indicate that the fault persists to the mantle (e.g., Shelly, 2010; Inbal et al., 2016) and the BDT occurs below the Moho, corresponding perhaps to the behavior predicted by our simulations without shear heating and with the coolest geotherms and/or elevated pore pressure. Alternatively, the ductile shear zone in the lower crust may be highly localized, a structure which is not predicted by any of our simulations. Our model predicts shear zones of about 1–5 km width in the lower crust and uppermost mantle, and we find that the width of the shear zone changes little with the inclusion of shear heating, consistent with results in Zhang & Sagiya (2017), and with scaling arguments in Montési & Zuber (2002), Montési (2013), and Moore & Parsons (2015). Significantly localized ductile shear zones would seem to require additional weakening mechanisms, such as foliation and fabric development (Bercovici & Karato, 2002; Montési, 2013).

5 Conclusions

In conclusion, we have developed a numerical method for simulating earthquake cycles with rate-and-state fault friction and off-fault power-law viscoelasticity, accounting for temperature evolution through a fully coupled thermomechanical framework. We investigated the interaction between the seismogenic zone, interseismic fault creep, and bulk viscous flow in the context of a continental strike-slip fault. We considered a range of ambient geotherms, parameterized by the lithosphere-asthenosphere boundary depth, hydrostatic or elevated pore fluid pressures along the fault, and frictional shear zone widths ranging over two orders of magnitude. We found that the transient temperature changes from shear heating can be neglected, and that model results such as the interseismic thermal anomaly and depth of the BDT are well-characterized by a steady-state approximation. Additionally, we find that both frictional and viscous shear heating contributed significantly to the total thermal energy of the system, and neither can be neglected.

We find that contributions to the thermal anomaly from frictional and viscous shear heating are of roughly equal magnitude, though the contribution from viscous shear heating is generally deeper and more broadly distributed. Frictional shear heating produces transient changes in temperature in the mid-crust in the coseismic and postseismic period, which for small frictional shear zone widths can reach hundreds of degrees Celsius. But most results are insensitive to these temperature changes, as a result of the short lifespan and limited spatial extent of the transient temperature rise. Additionally, features like the interseismic thermal anomaly and the depth of the BDT are well-characterized by a steady-state approximation, in which the effects of earthquake cycles are approximated with time-independent slip velocity and viscous strain rates. And in fact, cycle simulations which use the steady-state thermal anomaly and neglect transient shear heating effects all together produce very similar results to those which include the transient effects, at a significant reduction in computational cost.

6 Acknowledgements

This research was supported by the U.S. Geological Survey (G17AP00013), the National Science Foundation (EAR-1947448), and the Southern California Earthquake Center (Contribution No. 18050). SCEC is funded by NSF Cooperative Agreement EAR-1600087 & USGS Cooperative Agreement G17AC00047. The source code is available at https://bitbucket.org/kallison/scycle. Simulation data and input files used for this study can be found at osf.io/NZMW2/.

Appendix A Spin-up Procedure and Steady-State Solution using a Fixed Point Iteration Method

Earthquake cycle simulations typically must be spun up over many earthquake cycles to achieve system behavior that is independent of the selection of initial conditions (e.g., Takeuchi & Fialko, 2012; Allison & Dunham, 2018). For the parameters considered in this study, the cycle simulations ultimately reach a limit cycle, and all results reported pertain to this spun-up state. Spinning up viscoelastic earthquake cycle simulations with shear heating through brute force time integration is computationally infeasible due to the magnitude of the timescales involved.

There are two timescales relevant to the spin-up process. One is the timescale for the diffusion of heat,

$$T_{\text{th}} = \frac{L^2}{\alpha_{th}}, \tag{A1}$$

where L is the maximum length scale of interest, say the seismogenic zone thickness; taking $L \approx 20$ km we estimate $T_{\text{th}} \approx 12$ Ma. The second is the Maxwell time,

$$T_{\text{Max}} = \frac{\eta_{\text{eff}}}{\mu}, \tag{A2}$$

which varies by many orders of magnitude with depth, but can be as large as 1 Ma in the lower crust far from the ductile shear zone. These timescales are both so large that it is not computationally feasible to spin the system up through direct simulation of tens of thousands of earthquake cycles, so we have created a fixed point iteration method to solve for steady-state conditions (such as the steady-state shear stress, viscous strain rates, and temperature) which can be used as initial conditions for a cycle simulation. The steady state solution then serves as an initial condition for cycle simulations. This approach considerably shortens the spin-up time needed, though we find that even when starting from the steady-state solution, the cycle simulation must still be integrated through 50-100 earthquake cycles to reach the limit cycle solution in which elastic strain does not increase across successive cycles.

See Supporting Information (Figures S5 and S6) for an comparison between steady-state and cycle-averaged results.

Here we provide more details on the steady state solution method. We define steady state as when the elastic strain rates, and hence stress rates, are zero,

$$\dot{\sigma}_{xy} = 0, \quad \dot{\sigma}_{xz} = 0, \tag{A3}$$

or, equivalently, when viscous strains and particle displacements increase linearly with time,

$$\gamma_{xy} = \dot{\gamma}^V_{xy} t + \gamma^{V,0}_{xy}, \tag{A4}$$

$$\gamma_{xz} = \dot{\gamma}^V_{xz} t + \gamma^{V,0}_{xz}, \tag{A5}$$

$$u = vt + u_0, \tag{A6}$$

where $\gamma^{V,0}_{xy}$, $\gamma^{V,0}_{xz}$, and u_0 are the initial viscous strains and displacement, respectively, and $v = \partial u/\partial t$ is the particle velocity. Combining (A4)-(A6) with Hooke's law (2), produces

$$\sigma_{xy} = \mu \left(\frac{\partial u_0}{\partial y} - \gamma^{V,0}_{xy} \right), \quad \sigma_{xz} = \mu \left(\frac{\partial u_0}{\partial z} - \gamma^{V,0}_{xz} \right). \tag{A7}$$

We set $u_0 = 0$ without loss of generality, resulting in

$$\sigma_{xy} = -\mu \gamma^{V,0}_{xz}, \quad \sigma_{xz} = -\mu \gamma^{V,0}_{xz}. \tag{A8}$$

Combining Hooke's law (2) and the power-law viscous flow law (3) with Equation (A3) results in

$$\sigma_{xy} = \eta_{\text{eff}} \frac{\partial v}{\partial y}, \quad \sigma_{xz} = \eta_{\text{eff}} \frac{\partial v}{\partial z} \tag{A9}$$

and

$$\dot{\gamma}_{xy} = \frac{\partial v}{\partial y}, \quad \dot{\gamma}_{xz} = \frac{\partial v}{\partial z}. \tag{A10}$$

Using this result, the momentum balance equation (1) can be expressed in terms of v as

$$\frac{\partial}{\partial y}\left(\eta_{\text{eff}}\frac{\partial v}{\partial y}\right) + \frac{\partial}{\partial z}\left(\eta_{\text{eff}}\frac{\partial v}{\partial z}\right) = 0, \tag{A11}$$

subject to the boundary conditions

$$\sigma_{xy}(0,z) = \eta_{\text{eff}}\frac{\partial v}{\partial y}\bigg|_{y=0} = \tau_{ss}, \tag{A12}$$

$$v(L_y,z) = V_L/2, \tag{A13}$$

$$\sigma_{xz}(y,0) = \eta_{\text{eff}}\frac{\partial v}{\partial z}\bigg|_{z=0} = 0, \tag{A14}$$

$$\sigma_{xz}(y,L_z) = \eta_{\text{eff}}\frac{\partial v}{\partial z}\bigg|_{z=L_z} = 0, \tag{A15}$$

where $\tau_{ss}(V)$ is the steady-state shear stress on the fault.

We assume steady-state friction to evaluate $\tau_{ss}(V)$, but note that the steady-state slip velocity V is not necessarily equal to the loading velocity V_L (because viscous strain can also accommodate tectonic displacement), and must be determined as part of the solution to the steady-state problem. This formulation neglects the transient effects of earthquakes, providing an approximation to the cycle-averaged frictional strength of the fault. See Supplemental Information (Figure S6) for an illustration of this approximation. To solve for τ_{ss}, we use the method described in Allison & Dunham (2018) to integrate Equations (1)-(4) (the viscoelastic momentum balance equation), (11)-(10) (boundary conditions), and the rate-and-state expression for $\tau_{ss}(V)$ until $\tau_{ss}(V)$ and V cease to change appreciably.

Given $\tau_{ss}(V)$, Equations (A9)-(A15) are a nonlinear set of equations for the steady-state effective viscosity, stresses, viscous strains, and viscous strain rates. We solve these equations using a fixed point iteration method, illustrated in the green box in Figure A1. First guess an initial effective viscosity η_{eff}^i, and use it to solve Equations (A9)-(A15). Then compute a new effective viscosity η_{eff} using Equation (4). Finally, compute an update for effective viscosity

$$\eta_{\text{eff}}^{i+1} = \alpha\eta_{\text{eff}} + (1-\alpha)\eta_{\text{eff}}^i, \tag{A16}$$

where α is a damping factor, and $0 < \alpha \leq 1$. If α is too large, the fixed point method may not converge to a steady-state effective viscosity. We find that $\alpha = 0.2$ works well for the parameters considered in this paper. We also find that Equations (A11)-(A15) produce a poorly conditioned linear system, due to the wide range of values taken by η_{eff}, spanning many orders of magnitude. To remedy this, we impose a ceiling on the effective viscosity, $\eta_{\max} = 10^{26}$ Pa s, using the harmonic average

$$\eta_{\text{eff}}^{-1} = \eta_{\text{dis}}^{-1} + \eta_{\max}^{-1}, \tag{A17}$$

where η_{dis} is the effective viscosity resulting from dislocation creep in Equation (4). We find that varying $\eta_{\max}$ over 3 orders of magnitude does not change our results for the steady-state shear stress on the fault and its deep extension, nor the steady-state thermal anomaly.

Given the steady-state shear stress and effective viscosity, the steady-state temperature perturbation can be computed from

$$\frac{\partial}{\partial y}\left(k\frac{\partial \Delta T_{ss}}{\partial y}\right) + \frac{\partial}{\partial z}\left(k\frac{\partial \Delta T_{ss}}{\partial z}\right) + Q_{\text{visc}} + Q_{\text{fric}} = 0 \tag{A18}$$

with the previously stated boundary conditions. We also use a damping factor β to update the temperature perturbation

$$\Delta T_{ss}^{j+1} = \beta \Delta T_{ss} + (1-\beta)\Delta T_{ss}^{j}. \tag{A19}$$

We find that convergence of the overall fixed point system is more sensitive to β than α, and use $\beta = 0.15$.

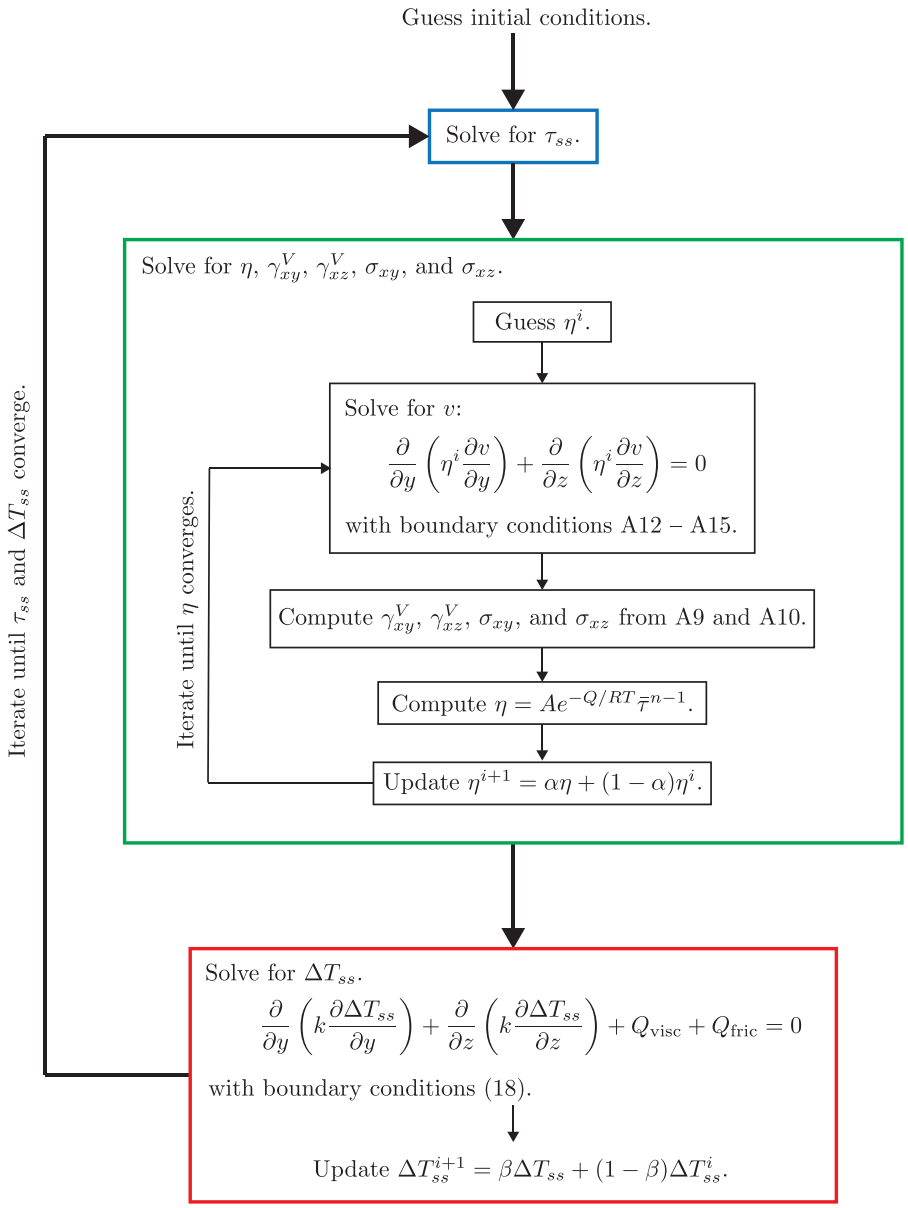

Figure A1. Illustration of the fixed point iteration method used to compute the steady-state solution.

References

Aagaard, B. T., Knepley, M. G., & Williams, C. A. (2013). A domain decomposi-

tion approach to implementing fault slip in finite-element models of quasi-static and dynamic crustal deformation. *Journal of Geophysical Research: Solid Earth*, *118*(6), 3059–3079. Retrieved from http://doi.wiley.com/10.1002/jgrb.50217 doi: 10.1002/jgrb.50217

Aharonov, E., & Scholz, C. H. (2018). A Physics-Based Rock Friction Constitutive Law: Steady State Friction. *Journal of Geophysical Research: Solid Earth*, *123*(2), 1591–1614. doi: 10.1002/2016JB013829

Aharonov, E., & Scholz, C. H. (2019). The Brittle-Ductile Transition Predicted by a Physics-Based Friction Law. *Journal of Geophysical Research: Solid Earth*, *124*(3), 2721–2737. doi: 10.1029/2018JB016878

Allison, K. L., & Dunham, E. M. (2018). *Earthquake cycle simulations with rate-and-state friction and power-law viscoelasticity* (Vol. 733). doi: 10.1016/j.tecto.2017.10.021

Allison, K. L., & Montesi, L. G. (2020). *Three definitions of ductile shear zones resulting from grain-size evolution below a frictional fault — Southern California Earthquake Center.* Retrieved from https://www.scec.org/publication/10222

Andrews, D. J. (2002). A fault constitutive relation accounting for thermal pressurization of pore fluid. *Journal of Geophysical Research: Solid Earth*, *107*(B12), ESE 15–1–ESE 15–8. Retrieved from http://doi.wiley.com/10.1029/2002JB001942 doi: 10.1029/2002JB001942

Barbot, S. D., & Fialko, Y. (2010). A unified continuum representation of post-seismic relaxation mechanisms: Semi-analytic models of afterslip, poroelastic rebound and viscoelastic flow. *Geophysical Journal International*, *182*(3), 1124–1140. doi: 10.1111/j.1365-246X.2010.04678.x

Barbot, S. D., Lapusta, N., & Avouac, J.-P. (2012). Under the hood of the earthquake machine: Toward predictive modeling of the seismic cycle. *Science*, *336*(May), 707–710. doi: 10.1126/science.1218796

Beeler, N. M., Hirth, G., Tullis, T. E., & Webb, C. H. (2018). On the depth extent of coseismic rupture. *Bulletin of the Seismological Society of America*, *108*(2), 761–780. Retrieved from https://pubs.geoscienceworld.org/ssa/bssa/article/108/2/761/528132/On-the-Depth-Extent-of-Coseismic-RuptureOn-thehttps://pubs.geoscienceworld.org/ssa/bssa/article/528132/On-the-Depth-Extent-of-Coseismic-RuptureOn-the doi: 10.1785/0120160295

Behr, W. M., & Hirth, G. (2014). Rheological properties of the mantle lid beneath the Mojave region in southern California. *Earth and Planetary Science Letters*, *393*, 60–72. doi: 10.1016/j.epsl.2014.02.039

Behr, W. M., & Platt, J. P. (2014). Brittle faults are weak, yet the ductile middle crust is strong: Implications for lithospheric mechanics. *Geophysical Research Letters*, *41*(22), 8067–8075. Retrieved from http://doi.wiley.com/10.1002/2014GL061349http://onlinelibrary.wiley.com/doi/10.1002/2014GL061349/pdf doi: 10.1002/2014GL061349

Bell, T. H. (1978). Progressive deformation and reorientation of fold axes in a ductile mylonite zone: the Woodroffe Thrust. *Tectonophysics*, *44*, 285–320. Retrieved from https://ac-els-cdn-com.stanford.idm.oclc.org/0040195178900744/1-s2.0-0040195178900744-main.pdf?{_}tid=3d79be56-c57b-4204-b779-bc24962d5605{\&}acdnat=1533234414{_}2430183e14bb61e8b2192712b56fc1d4

Bercovici, D., & Karato, S.-i. (2002). Theoretical Analysis of Shear Localization in the Lithosphere. *Reviews in Mineralogy and Geochemistry*, *51*(1), 387–420. Retrieved from https://pubs.geoscienceworld.org/rimg/article/51/1/387-420/87454 doi: 10.2138/gsrmg.51.1.387

Berthe, D., Choukroune, P., Jegouz, P., & Jegouzo, P. (1979). Orthogneiss, mylonite and non coaxial deformation of granites: the example of the

905 South Armorican Shear Zone. *Journal of Structural Geology*, *1*(1), 31–
906 42. Retrieved from https://ac-els-cdn-com.stanford.idm.oclc.org/
907 0191814179900191/1-s2.0-0191814179900191-main.pdf?{_}tid=
908 511706f1-2524-4578-9ffd-ed21d02d1563{\&}acdnat=1533210211{\
909 _}c311d344a1c796706105bb67b50db1a1
910 Blanpied, M. L., Lockner, D. A., & Byerlee, J. D. (1991). Fault stability inferred
911 from granite sliding experiments at hydrothermal conditions. *Geophysical Re-*
912 *search Letters*, *18*(4), 609–612. Retrieved from http://doi.wiley.com/10.1029/
913 91GL00469 doi: 10.1029/91GL00469
914 Blanpied, M. L., Lockner, D. A., & Byerlee, J. D. (1995). Frictional slip of granite at
915 hydrothermal conditions. *Journal of Geophysical Research: Solid Earth*, *100*(B7).
916 doi: 10.1029/95JB00862
917 Brace, W. F., & Kohlstedt, D. L. (1980). Limits on lithospheric stress imposed
918 by laboratory experiments. *Journal of Geophysical Research*, *85*(B11), 6248–
919 6252. Retrieved from http://doi.wiley.com/10.1029/JB085iB11p06248 doi:
920 10.1029/JB085iB11p06248
921 Bürgmann, R., & Dresen, G. (2008). Rheology of the lower crust and upper mantle:
922 Evidence from rock mechanics, geodesy, and field observations. *Annual Review*
923 *of Earth and Planetary Sciences*, *36*(1), 531–567. Retrieved from http://www
924 .annualreviews.org/doi/10.1146/annurev.earth.36.031207.124326http://
925 www.annualreviews.org/doi/abs/10.1146/annurev.earth.36.031207.124326
926 doi: 10.1146/annurev.earth.36.031207.124326
927 Byerlee, J. (1978). Friction of rocks. *Pure and Applied Geophysics*, *116*(4-5), 615–
928 626. Retrieved from http://link.springer.com/10.1007/BF00876528 doi: 10
929 .1007/BF00876528
930 Byerlee, J. (1990). Friction, overpressure and fault normal compression. *Geophysi-*
931 *cal Research Letters*, *17*(12), 2109–2112. Retrieved from http://doi.wiley.com/
932 10.1029/GL017i012p02109 doi: 10.1029/GL017i012p02109
933 Camacho, A., McDougall, I., Armstrong, R., & Braun, J. (2001). Evidence for shear
934 heating, Musgrave Block, central Australia. *Journal of Structural Geology*, *23*(6-
935 7), 1007–1013. doi: 10.1016/S0191-8141(00)00172-3
936 Camacho, A., Vernon, R. H., & Fitz Gerald, J. D. (1995). Large vol-
937 umes of anhydrous pseudotachylyte in the Woodroffe Thrust, eastern Mus-
938 grave Ranges, Australia. *Journal of Structural Geology*, *17*(3), 371 –
939 383. Retrieved from https://ac-els-cdn-com.stanford.idm.oclc.org/
940 019181419400069C/1-s2.0-019181419400069C-main.pdf?{_}tid=
941 057c512d-c053-4761-a44b-28e5f82ad3aa{\&}acdnat=1533233965{\
942 _}33d67765530637efee4eb385303ec6d1
943 Cattania, C. (2019). Complex Earthquake Sequences On Simple Faults. *Geophysical*
944 *Research Letters*, *46*(17-18), 10384–10393. doi: 10.1029/2019GL083628
945 Chatzaras, V., Tikoff, B., Newman, J., Withers, A. C., & Drury, M. R. (2015). Man-
946 tle strength of the San Andreas fault system and the role of mantle-crust feed-
947 backs. *Geology*, *43*(10), 891–894. Retrieved from http://geology.gsapubs.org/
948 lookup/doi/10.1130/G36752.1 doi: 10.1130/G36752.1
949 Chester, F. M. (1995). A rheologic model for wet crust applied to strike slip faults.
950 *Journal of Geophysical Research-Solid Earth*, *100*(B7), 13033–13044. Retrieved
951 from http://doi.wiley.com/10.1029/95JB00313 doi: 10.1029/95JB00313
952 Chester, F. M., & Chester, J. S. (1998). Ultracataclasite structure and friction pro-
953 cesses of the Punchbowl Fault, San Andreas system, California. *Tectonophysics*,
954 *295*(1), 199–221. Retrieved from http://www.sciencedirect.com/science/
955 article/pii/S0040195198001218 doi: 10.1016/S0040-1951(98)00121-8
956 Chester, F. M., Chester, J. S., Kirschner, D. L., Schulz, S. E., & Evans, J. P. (2004).
957 Structure of large-displacement, strike-slip fault zones in the brittle continental
958 crust. In G. D. Karner, B. Taylor, N. W. Driscoll, & D. L. Kohlstedt (Eds.), *Rhe-*

ology and deformation in the lithosphere at continetnal margins (pp. 223 – 260). New York: Columbia University Press.

Cole, J., Hacker, B., Ratschbacher, L., Dolan, J., Seward, G., Frost, E., & Frank, W. (2007). Localized ductile shear below the seismogenic zone: Structural analysis of an exhumed strike-slip fault, Austrian Alps. *Journal of Geophysical Research*, *112*(B12). Retrieved from http://doi.wiley.com/10.1029/2007JB004975 doi: 10.1029/2007JB004975

Dieterich, J. H. (1978). Time-dependent friction and the mechanics of stick-slip. *Pure and Applied Geophysics*, *116*(4-5), 790–806. Retrieved from http://link.springer.com/10.1007/BF00876539 doi: 10.1007/BF00876539

Dieterich, J. H. (1979). Modeling of rock friction 1. Experimental results and constitutive equations. *Journal of Geophysical Research: Solid Earth*, *84*(B5), 2161–2168. Retrieved from http://doi.wiley.com/10.1029/JB084iB05p02161 doi: 10.1029/JB084iB05p02161

Duru, K., Allison, K. L., Rivet, M., & Dunham, E. M. (2019). Dynamic rupture and earthquake sequence simulations using the wave equation in second-order form. *Geophysical Journal International*, *219*(2), 796–815. doi: 10.1093/gji/ggz319

England, P. (1993). The Interpretation of inverted metamorphic isograds using simple phyiscal calculations. *Tectonics*, *12*(1), 145–157.

Erickson, B. A., & Dunham, E. M. (2014). An efficient numerical method for earthquake cycles in heterogeneous media: Alternating subbasin and surface-rupturing events on faults crossing a sedimentary basin. *Journal of Geophysical Research: Solid Earth*, *119*(4), 3290–3316. Retrieved from http://doi.wiley.com/10.1002/2013JB010614 doi: 10.1002/2013JB010614

Erickson, B. A., Jiang, J., Barall, M., Lapusta, N., Dunham, E. M., Harris, R., ... Wei, M. (2020). The Community Code Verification Exercise for Simulating Sequences of Earthquakes and Aseismic Slip (SEAS). *Seismological Research Letters*, *91*(2A), 1–40. doi: 10.1785/0220190248

Freed, A. M., & Bürgmann, R. (2004). Evidence of power-law flow in the Mojave desert mantle. *Nature*, *430*, 548–551.

Frost, E., Dolan, J., Ratschbacher, L., Hacker, B., & Seward, G. (2011). Direct observation of fault zone structure at the brittle-ductile transition along the Salzach-Ennstal-Mariazell-Puchberg fault system, Austrian Alps. *Journal of Geophysical Research: Solid Earth*, *116*(2). Retrieved from http://doi.wiley.com/10.1029/2010JB007719 doi: 10.1029/2010JB007719

Fulton, P. M., & Saffer, D. M. (2009). Potential role of mantle-derived fluids in weakening the San Andreas Fault. *Journal of Geophysical Research: Solid Earth*, *114*(7), 1–15. doi: 10.1029/2008JB006087

Fulton, P. M., Saffer, D. M., Harris, R. N., & Bekins, B. A. (2004). Re-evaluation of heat flow data near Parkfield, CA: Evidence for a weak San Andreas Fault. *Geophysical Research Letters*, *31*(15), L15S15. Retrieved from http://doi.wiley.com/10.1029/2003GL019378 doi: 10.1029/2003GL019378

Gilley, L. D., Harrison, T. M., Leloup, P. H., Ryerson, F. J., Lovera, O. M., & Wang, J.-H. (2003). Direct dating of left-lateral deformation along the Red River shear zone, China and Vietnam. *Journal of Geophysical Research: Solid Earth*, *108*(B2). doi: 10.1029/2001jb001726

Goetze, C., & Evans, B. (1979). Stress and temperature in the bending lithosphere as constrained by experimental rock mechanics. *Geophysical Journal International*, *59*(3), 463–478. Retrieved from https://academic.oup.com/gji/article-lookup/doi/10.1111/j.1365-246X.1979.tb02567.xhttp://gji.oxfordjournals.org/content/59/3/463.short doi: 10.1111/j.1365-246X.1979.tb02567.x

Griffith, W. A., Di Toro, G., Pennacchioni, G., & Pollard, D. D. (2008). Thin pseudotachylytes in faults of the Mt. Abbot quadrangle, Sierra Nevada: Physical

constraints for small seismic slip events. *Journal of Structural Geology*, *30*(9), 1086–1094. doi: 10.1016/j.jsg.2008.05.003

Han, L., Hole, J. A., Stock, J. M., Fuis, G. S., Kell, A., Driscoll, N. W., ... Lázaro-Mancilla, O. (2016). Continental rupture and the creation of new crust in the Salton Trough rift, Southern California and northern Mexico: Results from the Salton Seismic Imaging Project. *Journal of Geophysical Research: Solid Earth*, *121*(10), 7469–7489. doi: 10.1002/2016JB013139

Hanmer, S. (1988). Great Slave Lake Shear Zone, Canadian Shield: reconstructed vertical profile of a crustal-scale fault zone. *Tectonophysics*, *149*(3-4), 245–264. doi: 10.1016/0040-1951(88)90176-X

Henstock, T. J., Levander, A., & Hole, J. A. (1997). Deformation in the lower crust of the San Andreas Fault System in Northern California. *Science*, *278*(5338), 650–653. Retrieved from `http://www.sciencemag.org/cgi/doi/10.1126/science.278.5338.650http://www.sciencemag.org/content/278/5338/650.abstract{\%}5Cnhttp://www.sciencemag.org/content/278/5338/650.full.pdf` doi: 10.1126/science.278.5338.650

Hirth, G., & Kohlstedt, D. L. (2003). Rheology of the upper mantle and the mantle wedge: A view from the experimentalists. *Geophysical Monograph Series*, *138*, 83–105. doi: 10.1029/138GM06

Hu, J., & Sun, Q. (2020). The effect of high temperature and pressure on rock friction coefficient: a review. *International Journal of Earth Sciences*, 1–11.

Hubbert, M. K., & Rubey, W. W. (1959). Role of fluid pressure in mechanics of overthrust faulting. *Bulletin of the Geological Society of America*, *70*, 115–166. Retrieved from `https://pubs.geoscienceworld.org/gsa/gsabulletin/article-pdf/70/2/115/3416670/i0016-7606-70-2-115.pdf`

Humphreys, E. D., & Hager, B. (1990). A kinematic model for the late Cenozoic development of southern California crust and upper mantle. *Journal of Geophysical Research-Solid Earth*, *95*(B12), 19747. Retrieved from `http://doi.wiley.com/10.1029/JB095iB12p19747papers3://publication/livfe/id/139152` doi: 10.1029/JB095iB12p19747

Inbal, A., Ampuero, J. P., & Clayton, R. W. (2016). Localized seismic deformation in the upper mantle revealed by dense seismic arrays. *Science*, *354*(6308), 88–93. Retrieved from `http://science.sciencemag.org/content/354/6308/88/tab-pdf` doi: 10.1126/science.aaf1370

Jackson, J. (2002). Strength of the continental lithosphere: Time to abandon the jelly sandwich? *GSA Today*, *12*(9), 4–10. doi: 10.1130/1052-5173(2002)012⟨0004:SOTCLT⟩2.0.CO;2

Jackson, J., McKenzie, D., Priestley, K., & Emmerson, B. (2008). New views on the structure and rheology of the lithosphere. *Journal of the Geological Society*, *165*(2), 453–465. doi: 10.1144/0016-76492007-109

Johnson, K. M., Hilley, G. E., & Bürgmann, R. (2007). Influence of lithosphere viscosity structure on estimates of fault slip rate in the Mojave region of the San Andreas Fault system. *Journal of Geophysical Research: Solid Earth*, *112*(7). Retrieved from `http://doi.wiley.com/10.1029/2006JB004842` doi: 10.1029/2006JB004842

Kaneko, Y., Ampuero, J. P., & Lapusta, N. (2011). Spectral-element simulations of long-term fault slip: Effect of low-rigidity layers on earthquake-cycle dynamics. *Journal of Geophysical Research: Solid Earth*, *116*(10). Retrieved from `http://doi.wiley.com/10.1029/2011JB008395` doi: 10.1029/2011JB008395

Kato, N. (2002). Seismic cycle on a strike-slip fault with rate- and state-dependent strength in an elastic layer overlying a viscoelastic half-space. *Earth, Planets and Space*, *54*(11), 1077–1083. Retrieved from `http://earth-planets-space.springeropen.com/articles/10.1186/BF03353305` doi: 10.1186/BF03353305

Kidder, S. B., Herman, F., Saleeby, J., Avouac, J. P., Ducea, M. N., & Chapman,

A. (2013). Shear heating not a cause of inverted metamorphism. *Geology*, *41*(8), 899–902. doi: 10.1130/G34289.1

Kirkpatrick, J. D., & Rowe, C. D. (2013). Disappearing ink: How pseudotachylytes are lost from the rock record. *Journal of Structural Geology*, *52*(1), 183–198. doi: 10.1016/j.jsg.2013.03.003

Klosko, E. R., Wu, F. T., Anderson, H. J., Eberhart-Phillips, D., McEvilly, T. V., Audoine, E., ... Gledhill, K. R. (1999). Upper mantle anisotropy in the New Zealand region. *Geophysical Research Letters*, *26*(10), 1497 – 1500. Retrieved from `http://doi.wiley.com/10.1029/1999GL900273c:{\%}5CUsers{\%}5CYifan{\%}5CDocuments{\%}5CReadCubeMedia{\%}5CGeophysicalResearchLetters1999KloskoE.pdf{\%}5Cnhttp://dx.doi.org/10.1029/1999GL900273https://s3.amazonaws.com/objects.readcube.com/articles/downloaded/wiley/4b` doi: 10.1029/1999GL900273

Lachenbruch, A. H., & Sass, J. H. (1977). Heat flow in the United States and the thermal regime of the crust. In J. Heacock, G. V. Keller, O. E., & G. Simmons (Eds.), *In the earth's crust.* American Geophysical Union (AGU). Retrieved from `http://doi.wiley.com/10.1029/GM020p0626` doi: 10.1029/GM020p0626

Lachenbruch, A. H., Sass, J. H., & Galanis, S. P. (1985). Heat flow in southernmost California and the origin of the Salton Trough. *Journal of Geophysical Research*, *90*(B8), 6709 – 6736. Retrieved from `http://doi.wiley.com/10.1029/JB090iB08p06709` doi: 10.1029/JB090iB08p06709

Lambert, V., & Barbot, S. (2016b). The role of thermal processes in defining the seismogenic zone: The interplay between faults and shear zones. *American Geophysical Union, Fall General Assembly 2016, abstract id. T22B-03*. Retrieved from `http://adsabs.harvard.edu/abs/2016AGUFM.T22B..03L`

Lambert, V., & Barbot, S. D. (2016a). Contribution of viscoelastic flow in earthquake cycles within the lithosphere-asthenosphere system. *Geophysical Research Letters*, *43*(19), 10,142–10,154. Retrieved from `http://doi.wiley.com/10.1002/2016GL070345` doi: 10.1002/2016GL070345.1.

Lapusta, N., & Rice, J. R. (2003a). Low-heat and low-stress fault operation in earthquake models of statically strong but dynamically weak faults. *American Geophysical Union, Fall Meeting 2003, abstract id. S51B-02*. Retrieved from `http://adsabs.harvard.edu/abs/2003AGUFM.S51B..02L`

Lapusta, N., & Rice, J. R. (2003b). Nucleation and early seismic propagation of small and large events in a crustal earthquake model. *Journal of Geophysical Research: Solid Earth*, *108*(B4). Retrieved from `http://doi.wiley.com/10.1029/2001JB000793` doi: 10.1029/2001JB000793

Lapusta, N., Rice, J. R., Ben-Zion, Y., & Zheng, G. (2000). Elastodynamic analysis for slow tectonic loading with spontaneous rupture episodes on faults with rate- and state-dependent friction. *Journal of Geophysical Research: Solid Earth*, *105*(B10), 23765–23789. Retrieved from `http://doi.wiley.com/10.1029/2000JB900250` doi: 10.1029/2000JB900250

Lekic, V., French, S. W., & Fisher, K. M. (2011). Lithospheric thinning beneath rifted regions of southern California. *Science*, *334*, 783 – 787.

Leloup, P., Arnaud, N., Lacassin, R., Kienast, J. R., Harrison, T., Phan Trong, T. T., ... Tapponnier, P. (2001). New constraints on the structure, thermochronology, and timing of the Ailao Shan-Red River shear zone, SE Asia. *Journal of Geophysical Research: Solid Earth*, *106*(B4), 6683–6732. doi: 10.1029/2000jb900322

Leloup, P., & Kienast, J. R. (1993). High-temperature metamorphism in a major strike-slip shear zone: the Ailao Shan-Red River, People's Republic of China. *Earth and Planetary Science Letters*, *118*(1-4), 213–234. doi: 10.1016/0012-821X(93)90169-A

Leloup, P., Ricard, Y., Battaglia, J., & Lacassin, R. (1999). Shear heating in con-

tinental strike-slip shear zones: Model and field examples. *Geophysical Journal International*, *136*(1), 19–40. Retrieved from https://academic.oup.com/gji/article-lookup/doi/10.1046/j.1365-246X.1999.00683.x doi: 10.1046/j.1365-246X.1999.00683.x

Leloup, P., Tapponnier, P., Lacassin, R., & Searle, M. (2007). Discussion on the role of the Red River shear zone, Yunnan and Vietnam, in the continental extrusion of SE Asia Journal, Vol. 163, 2006, 1025–1036. *Journal of the Geological Society*, *164*(6), 1253-1260. Retrieved from https://doi.org/10.1144/0016-76492007-065 doi: 10.1144/0016-76492007-065

Lemiszki, P. J., & Brown, L. D. (1988). Variable crustal structure of strike-slip fault zones as observed on deep seismic reflection profiles. *Bulletin of the Geological Society of America*, *100*(5), 665–676. Retrieved from http://gsabulletin.gsapubs.org/cgi/doi/10.1130/0016-7606(1988)100{\%}3C0665:VCSOSS{\%}3E2.3.CO;2 doi: 10.1130/0016-7606(1988)100⟨0665:VCSOSS⟩2.3.CO;2

Lin, A., Maruyama, T., Aaron, S., Michibayashi, K., Camacho, A., & Kano, K.-i. (2005). Propagation of seismic slip from brittle to ductile crust: Evidence from pseudotachylyte of the Woodroffe thrust, central Australia. *Tectonophysics*, *402*(1-4), 21–35. Retrieved from https://www.sciencedirect.com/science/article/pii/S004019510500137X doi: 10.1016/J.TECTO.2004.10.016

Lindsey, E. O., & Fialko, Y. (2016). Geodetic constraints on frictional properties and earthquake hazard in the Imperial Valley, southern California. *Journal of Geophysical Research B: Solid Earth*, *121*(2), 1097–1113. Retrieved from http://onlinelibrary.wiley.com/store/10.1002/2015JB012516/asset/jgrb51460.pdf?v=1{\&}t=j2a5b4b4{\&}s=5e1cb5d2e4cb866bbd855fd197d4048601908700 doi: 10.1002/2015JB012516

Liu, Y., McGuire, J. J., & Behn, M. D. (2012). Frictional behavior of oceanic transform faults and its influence on earthquake characteristics. *Journal of Geophysical Research: Solid Earth*, *117*(4). Retrieved from http://doi.wiley.com/10.1029/2011JB009025 doi: 10.1029/2011JB009025

Lyzenga, G. A., Raefsky, A., & Mulligan, S. G. (1991). Models of recurrent strike-slip earthquake cycles and the state of crustal stress. *Journal of Geophysical Research: Solid Earth*, *96*(B13), 21623–21640. Retrieved from http://doi.wiley.com/10.1029/91JB02260 doi: 10.1029/91JB02260

Maggi, A., Jackson, J. A., McKenzie, D., & Priestley, K. (2000). Earthquake focal depths, effective elastic thickness, and the strength of the continental lithosphere. *Geology*, *28*(6), 495–498. Retrieved from http://geology.gsapubs.org/cgi/doi/10.1130/0091-7613(2000)28{\%}3C495:EFDEET{\%}3E2.0.CO;2 doi: 10.1130/0091-7613(2000)28⟨495:EFDEET⟩2.0.CO;2

Marone, C. (1998). Laboratory-derived friction laws and their application to seismic faulting. *Annual Review of Earth and Planetary Sciences*, *26*(1), 643–696. Retrieved from http://www.annualreviews.org/doi/10.1146/annurev.earth.26.1.643 doi: 10.1146/annurev.earth.26.1.643

Marone, C., & Kilgore, B. (1993). Scaling of the critical slip distance for seismic faulting with shear strain in fault zones. *Nature*, *362*(6421), 618–621. Retrieved from http://www.nature.com/doifinder/10.1038/362618a0 doi: 10.1038/362618a0

Melosh, B. L., Rowe, C. D., Gerbi, C., Smit, L., & Macey, P. (2018). Seismic cycle feedbacks in a mid-crustal shear zone. *Journal of Structural Geology*, *112*, 95–111.

Miller, M. S., Zhang, P., & Dolan, J. F. (2014). Moho structure across the San Jacinto fault zone: Insights into strain localization at depth. *Lithosphere*, *6*(1), 43–47. Retrieved from http://lithosphere.gsapubs.org/cgi/doi/10.1130/L295.1 doi: 10.1130/L295.1

Mitchell, E. K., Fialko, Y., & Brown, K. M. (2016). Velocity-weakening behavior

of Westerly granite at temperature up to 600 C. *Journal of Geophysical Research: Solid Earth*, *121*(9), 6932–6946. Retrieved from http://doi.wiley.com/10.1002/2016JB013081 doi: 10.1002/2016JB013081

Miyake, Y., & Noda, H. (2019). Fully dynamic earthquake sequence simulation of a fault in a viscoelastic medium using a spectral boundary integral equation method: does interseismic stress relaxation promote aseismic transients? *Earth, Planets and Space*, *71*(1), 1–12.

Molnar, P. (1999). Continuous deformation versus faulting through the continental lithosphere of New Zealand. *Science*, *286*(5439), 516–519. Retrieved from http://www.sciencemag.org/cgi/doi/10.1126/science.286.5439.516 doi: 10.1126/science.286.5439.516

Montési, L. G. (2013). Fabric development as the key for forming ductile shear zones and enabling plate tectonics. *Journal of Structural Geology*, *50*, 254–266. Retrieved from http://linkinghub.elsevier.com/retrieve/pii/S0191814113000102 doi: 10.1016/j.jsg.2012.12.011

Montési, L. G., & Zuber, M. T. (2002). A unified description of localization for application to large-scale tectonics. *Journal of Geophysical Research*, *107*(B3). Retrieved from http://doi.wiley.com/10.1029/2001JB000465 doi: 10.1029/2001JB000465

Moore, J. D., & Parsons, B. (2015). Scaling of viscous shear zones with depth-dependent viscosity and power-law stress-strain-rate dependence. *Geophysical Journal International*, *202*(1), 242–260. Retrieved from http://academic.oup.com/gji/article/202/1/242/589272/Scaling-of-viscous-shear-zones-with-depthdependent doi: 10.1093/gji/ggv143

Neumann, F., Negrete-Aranda, R., Harris, R. N., Contreras, J., Sclater, J. G., & González-Fernández, A. (2017). Systematic heat flow measurements across the Wagner Basin, northern Gulf of California. *Earth and Planetary Science Letters*, *479*, 340–353. Retrieved from https://doi.org/10.1016/j.epsl.2017.09.037 doi: 10.1016/j.epsl.2017.09.037

Noda, H., Dunham, E. M., & Rice, J. R. (2009). Earthquake ruptures with thermal weakening and the operation of major faults at low overall stress levels. *Journal of Geophysical Research*, *114*. Retrieved from http://doi.wiley.com/10.1029/2008JB006143 doi: 10.1029/2008JB006143

Noda, H., & Lapusta, N. (2010). Three-dimensional earthquake sequence simulations with evolving temperature and pore pressure due to shear heating: Effect of heterogeneous hydraulic diffusivity. *Journal of Geophysical Research: Solid Earth*, *115*(B12314). Retrieved from http://doi.wiley.com/10.1029/2010JB007780 doi: 10.1029/2010JB007780

Noda, H., & Shimamoto, T. (2005). Thermal pressurization and slip-weakening distance of a fault: An example of the Hanaore fault, southwest Japan. *Bulletin of the Seismological Society of America*, *95*(4), 1224–1233. Retrieved from https://pubs.geoscienceworld.org/bssa/article/95/4/1224-1233/121052 doi: 10.1785/0120040089

Norris, R. J., & Cooper, A. F. (2003). Very high strains recorded in mylonites along the Alpine Fault, New Zealand: Implications for the deep structure of plate boundary faults. *Journal of Structural Geology*, *25*(12), 2141–2157. Retrieved from http://www.sciencedirect.com/science/article/pii/S0191814103000452 doi: 10.1016/S0191-8141(03)00045-2

Norris, R. J., & Toy, V. G. (2014). *Continental transforms: A view from the Alpine Fault* (Vol. 64). Pergamon. Retrieved from http://www.sciencedirect.com/science/article/pii/S0191814114000601 doi: 10.1016/j.jsg.2014.03.003

Petley-Ragan, A., Ben-Zion, Y., Austrheim, H., Ildefonse, B., Renard, F., & Jamtveit, B. (2019). Dynamic earthquake rupture in the lower crust. *Science advances*, *5*(7), eaaw0913.

Platt, J. P., & Behr, W. M. (2011). Deep structure of lithospheric fault zones. *Geophysical Research Letters*, *38*(24). Retrieved from http://doi.wiley.com/10.1029/2011GL049719 doi: 10.1029/2011GL049719

Rempel, A. W., & Rice, J. R. (2006). Thermal pressurization and onset of melting in fault zones. *Journal of Geophysical Research: Solid Earth*, *111*(B9).

Rice, J. R. (1992). Chapter 20 Fault Stress States, pore pressure distributions, and the weakness of the San Andreas Fault. *International Geophysics*, *51*(C), 475–503. Retrieved from http://linkinghub.elsevier.com/retrieve/pii/S0074614208628351 doi: 10.1016/S0074-6142(08)62835-1

Rice, J. R. (1993). Spatiotemporal complexity of slip on a fault. *Journal of Geophysical Research*, *98*(B6), 9885–9907. Retrieved from http://doi.wiley.com/10.1029/93JB00191 doi: 10.1029/93JB00191

Rice, J. R. (2006). Heating and weakening of faults during earthquake slip. *Journal of Geophysical Research: Solid Earth*, *111*(5). Retrieved from http://doi.wiley.com/10.1029/2005JB004006 doi: 10.1029/2005JB004006

Rice, J. R., Lapusta, N., & Ranjith, K. (2001). Rate and state dependent friction and the stability of sliding between elastically deformable solids. *Journal of the Mechanics and Physics of Solids*, *49*, 1865–1898. Retrieved from http://linkinghub.elsevier.com/retrieve/pii/S0022509601000424 doi: 10.1016/S0022-5096(01)00042-4

Rosenberg, C. L., & Schneider, S. (2008). The western termination of the SEMP Fault (eastern Alps) and its bearing on the exhumation of the Tauern Window. *Geological Society Special Publication*, *298*, 197–218. doi: 10.1144/SP298.10

Ruina, A. (1983). Slip instability and state variable friction laws. *Journal of Geophysical Research: Solid Earth*, *88*(B12), 10359–10370. Retrieved from http://doi.wiley.com/10.1029/JB088iB12p10359 doi: 10.1029/JB088iB12p10359

Rybacki, E., & Dresen, G. (2004). Deformation mechanism maps for feldspar rocks. *Tectonophysics*, *382*(3-4), 173–187. Retrieved from https://ac.els-cdn.com/S0040195104000186/1-s2.0-S0040195104000186-main.pdf?{_}tid=be6857c2-fb16-11e7-b706-00000aacb361{\&}acdnat=1516146264{_}dda4e347dad556b799c0dbf083f6075c doi: 10.1016/j.tecto.2004.01.006

Rybacki, E., Gottschalk, M., Wirth, R., & Dresen, G. (2006). Influence of water fugacity and activation volume on the flow properties of fine-grained anorthite aggregates. *Journal of Geophysical Research: Solid Earth*, *111*(B3), n/a–n/a. Retrieved from http://doi.wiley.com/10.1029/2005JB003663 doi: 10.1029/2005JB003663

Sass, J. H., Williams, C. F., Lachenbruch, A. H., Galanis, S. P. J., & Grubb, F. V. (1997). Thermal regime of the San Andreas fault near Parkfield, California. *Journal of Geophysical Research*, *102*, 27,527–575,586.

Savage, J. C., & Lachenbruch, A. H. (2003). Consequences of viscous drag beneath a transform fault. *Journal of Geophysical Research: Solid Earth*, *108*(B1). Retrieved from http://doi.wiley.com/10.1029/2001JB000711 doi: 10.1029/2001JB000711

Savage, J. C., & Prescott, W. H. (1978). Asthenosphere readjustment and the earthquake cycle. *Journal of Geophysical Research*, *83*(B7), 3369–3376. Retrieved from http://onlinelibrary.wiley.com/doi/10.1029/JB083iB07p03369/full doi: 10.1029/JB083iB07p03369

Searle, M. P., Yeh, M. W., Lin, T. H., & Chung, S. L. (2010). Structural constraints on the timing of left-lateral shear along the red river shear zone in the ailao shan and diancang shan ranges, Yunnan, SW China. *Geosphere*, *6*(4), 316–338. doi: 10.1130/GES00580.1

Shelly, D. R. (2010). Migrating tremors illuminate complex deformation beneath the seismogenic San Andreas fault. *Nature*, *463*(7281), 648–652. Retrieved from https://www.nature.com/nature/journal/v463/n7281//pdf/

nature08755.pdfhttp://www.ncbi.nlm.nih.gov/pubmed/20130648 doi: 10.1038/nature08755

Shimamoto, T., & Noda, H. (2014). A friction to flow constitutive law and its application to a 2-D modeling of earthquakes. *Journal of Geophysical Research: Solid Earth*, *119*(11), 8089–8106. Retrieved from http://doi.wiley.com/10.1002/2014JB011170 doi: 10.1002/2014JB011170

Sibson, R. H. (1974). Frictional constraints on thrust, wrench and normal faults. *Nature*, *249*, 542–544. Retrieved from http://www.nature.com/doifinder/10.1038/249542a0 doi: 10.1038/249542a0

Sibson, R. H. (1982). Fault zone models, heat flow, and the depth distribution of earthquakes in the continental crust of the United States. *Bulletin of the Seismological Society of America*, *72*(1), 151–163.

Sibson, R. H. (1984). Roughness at the base of the seismogenic zone: Contributing factors. *Journal of Geophysical Research*, *89*. doi: 10.1029/JB089iB07p05791

Sibson, R. H. (2003). Thickness of the seismic slip zone. *Bulletin of the Seismological Society of America*, *93*(3), 1169–1178. Retrieved from https://gsw.silverchair-cdn.com/gsw/Content{_}public/Journal/bssa/93/3/10.1785{_}0120020061/4/1169.pdf?Expires=2147483647{\&}Signature=Uzay8NnoHacPNXjjEaNsm5ZwsgOE3F{~}MWUdq2Es2wcb0jYCZwD4rDRkN25i0K{~}1pO5PjU{~}aAmWJDFQnLyPsdMhGgZGj-U3ax4S{~}k{~}zMxcJwv doi: 10.1785/0120020061

Sibson, R. H., & Toy, V. G. (2006). The habitat of fault-generated pseudotachylyte: Presence vs. absence of friction-melt. *Earthquakes: Radiated Energy and the Physics of Faulting*, 153–166. Retrieved from http://www.agu.org/books/gm/v170/170GM16/170GM16.shtml doi: 10.1029/170GM16

Takeuchi, C. S., & Fialko, Y. (2012). Dynamic models of interseismic deformation and stress transfer from plate motion to continental transform faults. *Journal of Geophysical Research*, *117*(B5), n/a–n/a. Retrieved from http://doi.wiley.com/10.1029/2011JB009056 doi: 10.1029/2011JB009056

Takeuchi, C. S., & Fialko, Y. (2013). On the effects of thermally weakened ductile shear zones on postseismic deformation. *Journal of Geophysical Research: Solid Earth*, *118*(12), 6295–6310. Retrieved from http://doi.wiley.com/10.1002/2013JB010215 doi: 10.1002/2013JB010215

Tembe, S., Lockner, D., & Wong, T. F. (2009). Constraints on the stress state of the San Andreas Fault with analysis based on core and cuttings from San Andreas Fault Observatory at Depth (SAFOD) drilling phases 1 and 2. *Journal of Geophysical Research: Solid Earth*, *114*(11). Retrieved from http://doi.wiley.com/10.1029/2008JB005883 doi: 10.1029/2008JB005883

Thatcher, W. (1983). Nonlinear strain buildup and the earthquake cycle on the San Andreas Fault. *Journal of Geophysical Research*, *88*(B7), 5893–5902. doi: 10.1029/JB088iB07p05893

Thatcher, W., & Chapman, D. (2018). Heat Flow Data and Seismic Imaging Reveal Both Transient and Steady-State Thermo-Mechanical Processes at Work Beneath Southern California. *AGU Fall Meeting Abstracts*, *2018*, T52D–08.

Thatcher, W., & England, P. C. (1998). Ductile shear zones beneath strike-slip faults: Implications for the thermomechanics or the San Andreas fault zone. *Journal of Geophysical Research*, *103*(B1), 891–905.

Thatcher, W., & Pollitz, F. F. (2008). Temporal evolution of continental lithospheric strength in actively deforming regions. *GSA Today*, *18*(4/5), 4–11. Retrieved from ftp://portcullis.earth.ox.ac.uk/pub/tony/mike/Thatcher{_}Pollitz{_}2007{_}submitted.pdf doi: 10.1130/GSATO1804-5A.1

Tse, S. T., & Rice, J. R. (1986). Crustal earthquake instability in relation to the depth variation of frictional slip properties. *Journal of Geophysical Research*, *91*(B9), 9452–9472. doi: 10.1029/JB091iB09p09452

Tullis, T. E., & Weeks, J. D. (1986). Constitutive behavior and stability of fric-

tional sliding of granite. *Pure and Applied Geophysics PAGEOPH*. doi: 10.1007/BF00877209

Turcotte, D. L., & Schubert, G. (2002). *Geodynamics* (2nd ed.). Cambridge University Press.

Vauchez, A., & Tommasi, A. (2003). Wrench faults down to the asthenosphere: geological and geophysical evidence and thermomechanical effects. *Geological Society, London, Special Publications*, *210*(1), 15–34. Retrieved from http://sp.lyellcollection.org/lookup/doi/10.1144/GSL.SP.2003.210.01.02 doi: 10.1144/GSL.SP.2003.210.01.02

Vissers, R. L. M., Drury, M. R., Newman, J., & Fliervoet, T. E. (1997). Mylonitic deformation in upper mantle peridotites of the North Pyrenean Zone (France): implications for strength and strain localization in the lithosphere. *Tectonophysics*, *279*, 303–325.

Warren, J. M., & Hirth, G. (2006). Grain size sensitive deformation mechanisms in naturally deformed peridotites. *Earth and Planetary Science Letters*, *248*(1-2), 423–435. Retrieved from http://www.sciencedirect.com/science/article/pii/S0012821X06004225 doi: 10.1016/j.epsl.2006.06.006

Weber, M., Abu-Ayyash, K., Abueladas, A., Agnon, A., Al-Amoush, H., Babeyko, A., ... Wylegalla, K. (2004). The crustal structure of the Dead Sea Transform. *Geophysical Journal International*, *156*, 655–681. Retrieved from https://oup.silverchair-cdn.com/oup/backfile/Content{_}public/Journal/gji/156/3/10.1111/j.1365-246X.2004.02143.x/2/156-3-655.pdf?Expires=1494900268{\&}Signature=O8gIFFx9boL7I9SHyBKLq{~}vUyDryZjC2dXdFYNgqEsPKERd8ZmOHrULPJtVEMlxxxvX4LTgM9Hy-DTElB9mOXEvUbOEBRRuyYvV doi: 10.1111/j.1365-246X.2004.02143.x

Weijermars, R. (1987). The Palomares brittle-ductile Shear Zone of southern Spain. *Journal of Structural Geology*, *9*(2), 130–157. Retrieved from https://ac-els-cdn-com.stanford.idm.oclc.org/0191814187900228/1-s2.0-0191814187900228-main.pdf?{_}tid=2c3d520d-d817-4e00-9c30-f5b15d8aead8{\&}acdnat=1533233889{_}82fddfcb8895a6699400bfe3ea8e2587

White, J. C. (2012). Paradoxical pseudotachylyte - Fault melt outside the seismogenic zone. *Journal of Structural Geology*, *38*, 11–20. Retrieved from http://dx.doi.org/10.1016/j.jsg.2011.11.016 doi: 10.1016/j.jsg.2011.11.016

Wibberley, C. A., & Shimamoto, T. (2002). Internal structure and permeability of major strike-slip fault zones: The Median Tectonic Line in Mie Prefecture, Southwest Japan. *Journal of Structural Geology*, *25*(1), 59–78. Retrieved from www.elsevier.com/locate/jsg doi: 10.1016/S0191-8141(02)00014-7

Williams, C. F., & DeAngelo, J. (2011). Evaluation of approaches and uncertainties in estimation of temperature in the upper crust of the western United States. *GRC Transactions*, *35*, 1599 – 1606.

Wilson, C. K., Jones, C. H., Molnar, P., Sheehan, A. F., & Boyd, O. S. (2004). Distributed deformation in the lower crust and upper mantle beneath a continental strike-slip fault zone: Marlborough Fault System, South Island, New Zealand. *Geology*, *32*(10), 837–840. Retrieved from http://geology.gsapubs.org/cgi/doi/10.1130/G20657.1http://geology.gsapubs.org/content/32/10/837.shorthttp://geology.gsapubs.org/content/32/10/837.full.pdf doi: 10.1130/G20657.1

Wright, T. J., Elliott, J. R., Wang, H., & Ryder, I. (2013). Earthquake cycle deformation and the Moho: Implications for the rheology of continental lithosphere. *Tectonophysics*, *609*, 504–523. Retrieved from http://dx.doi.org/10.1016/j.tecto.2013.07.029http://www.sciencedirect.com/science/article/pii/S0040195113004708 doi: 10.1016/j.tecto.2013.07.029

Yang, Y., & Forsyth, D. W. (2008). Attenuation in the upper mantle be-

neath southern California: Physical state of the lithosphere and asthenosphere. *Journal of Geophysical Research: Solid Earth*, *113*(3). Retrieved from http://doi.wiley.com/10.1029/2007JB005118 doi: 10.1029/2007JB005118

Zhang, X., & Sagiya, T. (2017). Shear strain concentration mechanism in the lower crust below an intraplate strike-slip fault based on rheological laws of rocks. *Earth, Planets and Space*, *69*(1). Retrieved from https://link.springer.com/content/pdf/10.1186{\%}2Fs40623-017-0668-5.pdf doi: 10.1186/s40623-017-0668-5

Zhu, L. (2000). Crustal structure across the San Andreas Fault, southern California from teleseismic converted waves. *Earth and Planetary Science Letters*, *179*, 183–190. Retrieved from http://ac.els-cdn.com/S0012821X00001011/1-s2.0-S0012821X00001011-main.pdf?{_}tid=60486596-3902-11e7-a44a-00000aacb360{\&}acdnat=1494806982{_}f5335d669505f121c0afc32db93f3935

Supporting Information for "Influence of Shear Heating and Thermomechanical Coupling on Earthquake Sequences and the Brittle-Ductile Transition"

Kali L. Allison[1,2], Eric M. Dunham[1,3]

[1]Department of Geophysics, Stanford University, Stanford, California, USA

[2]now at: Department of Geology, University of Maryland, College Park, Maryland, USA

[3]Institute for Computational and Mathematical Engineering, Stanford University, Stanford, California, USA

1. Numerical Method

The discretization of the governing equations is a straightforward extension of previous work. We employ the Cartesian grid finite difference method developed by Erickson & Dunham (2014) and Allison & Dunham (2018) to solve the static elasticity and heat equations, both on the same grid. We select the along-fault grid spacing to resolve the nucleation length (e.g., Ruina, 1983; Rice, 1983, 1993; Rice et al., 2001),

$$h^* = \frac{\mu d_c}{\sigma_n (b-a)} \tag{1}$$

and the cohesive-zone size (Dieterich, 1992; Ampuero & Rubin, 2008),

$$L_b = \frac{\mu d_c}{\sigma_n b}, \tag{2}$$

which is generally smaller than h^*. In the fault-normal direction, we must resolve thermal boundary layers near the fault, the width of which will be no larger than w. Therefore, we use a grid spacing of $L_b/4$ in the z-direction in the seismogenic zone, and $w/5$ in the y-direction near the fault, with aggressive grid stretching outside of this region.

We next explain time stepping. We utilize the explicit Runge–Kutta algorithm with adaptive time-step selection described in Allison & Dunham (2018) to update slip, state variable, and viscous strains. However, stiffness of the heat equation requires implicit time-stepping for efficiency. To handle this, we use operator splitting, updating temperature in the heat equation with backward Euler after each full adaptive step.

Specifically, during each adaptive Runge–Kutta time step from time t^n to $t^{n+1} = t^n + \Delta t$, temperature is held fixed at ΔT^n while solving for slip δ^{n+1}, state ψ^{n+1}, and the viscous strains γ_{xy}^{n+1} and γ_{xz}^{n+1}. We then compute the stresses at t^{n+1}, and the flow law provides the viscous strain rates $\dot{\gamma}_{xy}^{n+1}$ and $\dot{\gamma}_{xz}^{n+1}$. Then, these fields are held fixed and used to compute the shear heating source term Q^{n+1} when solving for ΔT^{n+1}.

2. Stresses

The similarities and differences between these three simulations featured in Figure 4 can also be seen in the temporal evolution of shear stress on the fault and its deep extension, plotted in Figure S1. In the upper crust, the shear stress is very similar in all three simulations, because the off-fault material is effectively elastic and stress is limited by the frictional strength of the fault. At greater depths, around 23 km in the viscoelastic simulation without shear heating and 15 km in the viscoelastic simulation with shear heating, the viscoelastic material becomes much weaker than the frictional strength of the fault, resulting in a much weaker shear stress than in the elastic simulation.

3. Influence of Pore Pressure on Contributions to Shear Heating

Figure S2 explores the influence of pore pressure, parametrized through λ, on the thermal anomaly.

4. Thermal Energy

One way of summarizing the results of our parameter space search is to integrate the thermal anomaly times the heat capacity over the domain, producing the thermal energy per unit length θ. As shown in Figure S3, the total thermal energy increases with deeper LAB depths. It also decreases slightly with increasing pore pressure, but this is a much smaller effect. Also, for all the parameters considered, both frictional and viscous shear heating contribute substantially to the total thermal energy in the system, with viscous shear heating constituting more than half the total (except for the simulation with a 70 km deep LAB and $\lambda = 0.8$).

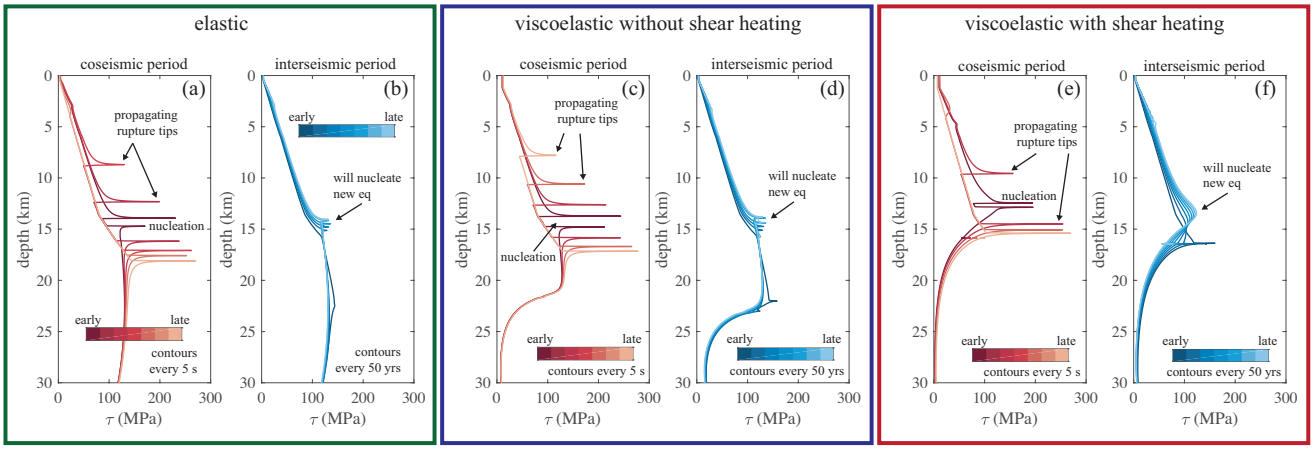

Figure S1. Comparison of the temporal evolution of shear stress on the fault and its deep extension in elastic, viscoelastic without shear heating, and viscoelastic with shear heating cycle simulations, for an LAB of 50 km and hydrostatic pore pressure. (a), (c) and (e) First 20 s of the coseismic period, with contours plotted every 5 s. (b), (d) and (f) Interseismic period with contours plotted every 50 years.

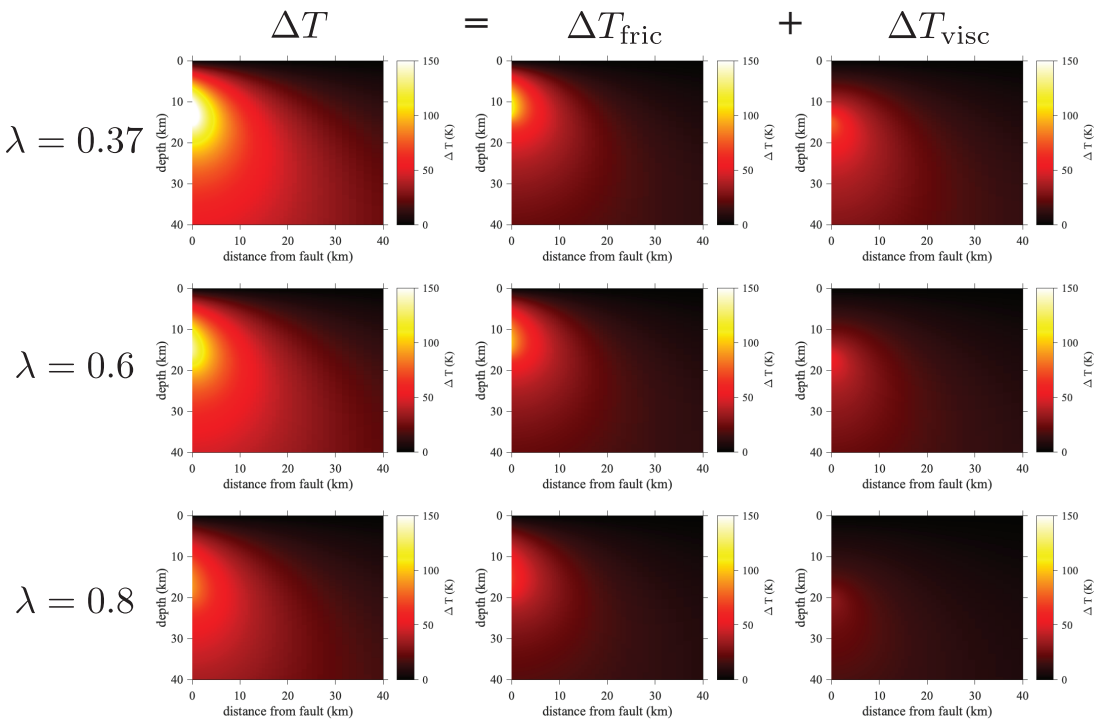

Figure S2. Comparison of ΔT and its components ΔT_{fric} and ΔT_{visc}, as a function of λ, for a simulation with a 50 km deep LAB.

5. Temperatures of Various Transitions

The temperatures which correspond with the depths plotted in Figure 8 are shown in Figure S4.

6. Comparison of Steady-State and Cycle-Averaged Results

Figures S5 and S6 compare steady-state and cycle-averaged results.

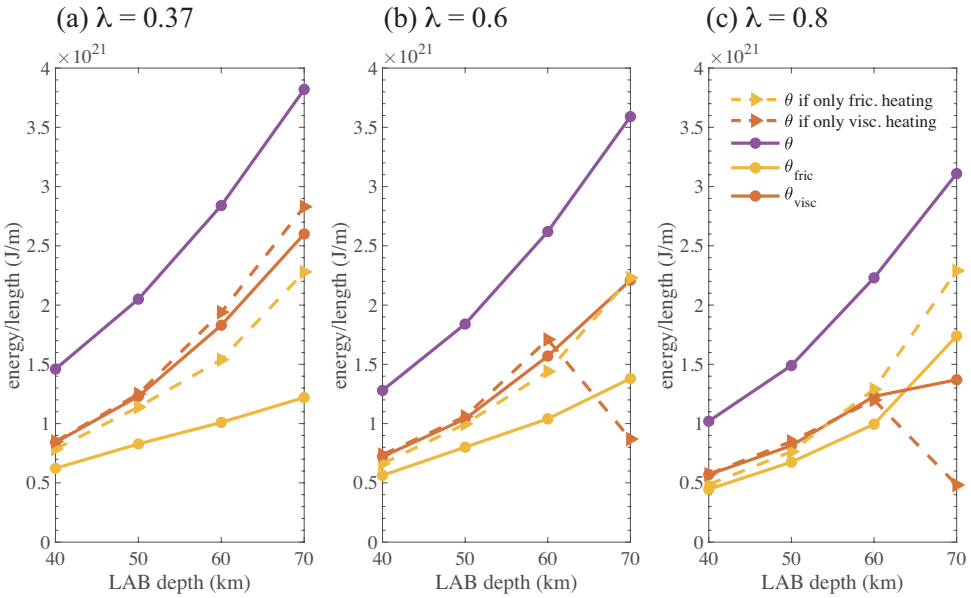

Figure S3. Total thermal energy θ (purple), portion of total thermal energy contributed by frictional θ_{fric} (yellow, solid lines) and viscous θ_{visc} (red, solid lines)) shear heating, total energy from simulations with only frictional shear heating (yellow, dashed lines), and total energy from simulations with only viscous shear heating (red, dashed lines), as a function of LAB depth and pore pressure.

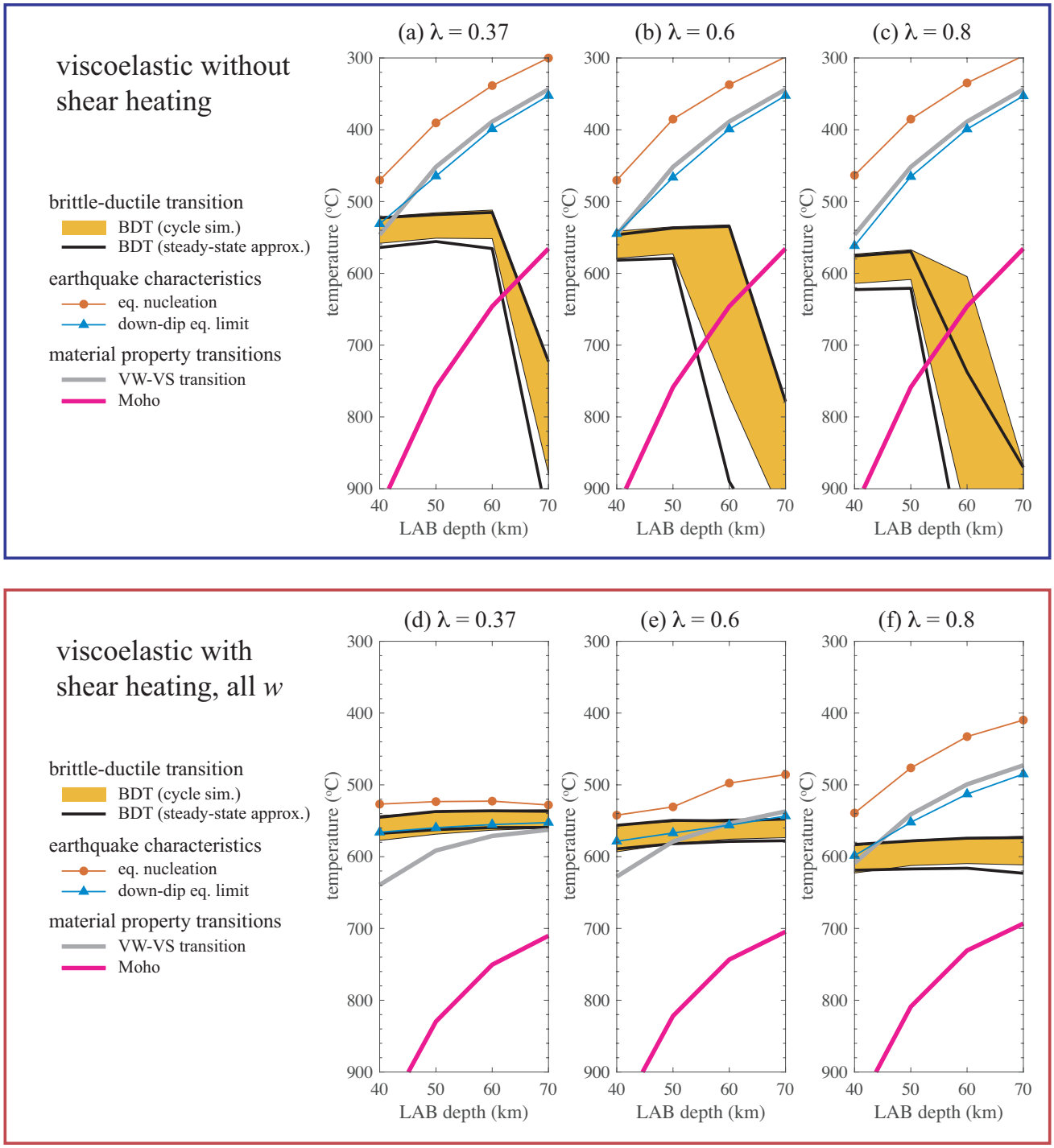

Figure S4. Comparison between the temperatures of earthquake nucleation (red circles), the down-dip limit of coseismic slip (blue triangles), and the BDT temperature range (yellow filled regions) for simulations with and without shear heating. For the viscoelastic simulations with shear heating, the average interseismic temperature is used. Also shown are estimates of the BDT temperatures from steady-state results (black lines).

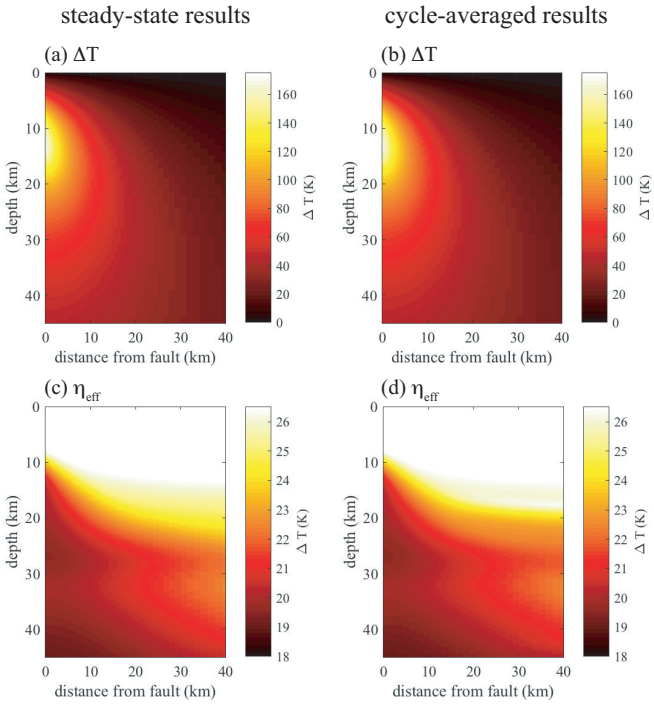

Figure S5. Comparison between steady-state and cycle-averaged results: thermal anomaly (a and b), and effective viscosity (c and d). Results are for a 50 km deep LAB and hydrostatic pore pressure.

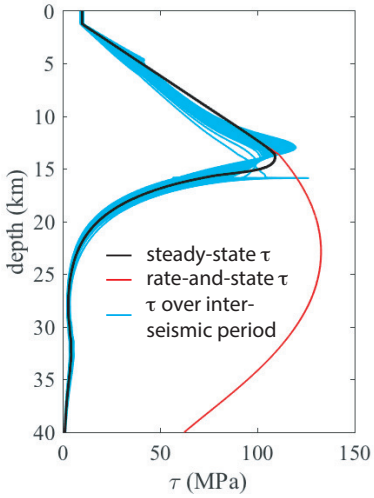

Figure S6. The steady-state shear stress on the fault and its deep extension (black) shows good agreement with the interseismic shear stress (blue) for a viscoelastic cycle simulation with shear heating, with a 50 km deep LAB and $\lambda = 0.37$. Also shown, for reference, is the shear stress for rate-and-state friction assuming the fault is sliding at the tectonic loading velocity (red).

References

Allison, K. L., & Dunham, E. M. (2018). *Earthquake cycle simulations with rate-and-state friction and power-law viscoelasticity* (Vol. 733). doi: 10.1016/j.tecto.2017.10.021

Ampuero, J.-P., & Rubin, A. M. (2008). Earthquake nucleation on rate and state faults - Aging and slip laws. *Journal of Geophysical Research*, *113*(B1). Retrieved from http://doi.wiley.com/10.1029/2007JB005082 doi: 10.1029/2007JB005082

Dieterich, J. H. (1992). Earthquake nucleation on faults with rate-and state-dependent strength. *Tectonophysics*, *211*(1), 115–134. doi: 10.1016/0040-1951(92)90055-B

Erickson, B. A., & Dunham, E. M. (2014). An efficient numerical method for earthquake cycles in heterogeneous media: Alternating subbasin and surface-rupturing events on faults crossing a sedimentary basin. *Journal of Geophysical Research: Solid Earth*, *119*(4), 3290–3316. Retrieved from http://doi.wiley.com/10.1002/2013JB010614 doi: 10.1002/2013JB010614

Rice, J. R. (1983). Constitutive relations for fault slip and earthquake instabilities. *Pure and Applied Geophysics PAGEOPH*, *121*(3), 443–475. doi: 10.1007/BF02590151

Rice, J. R. (1993). Spatiotemporal complexity of slip on a fault. *Journal of Geophysical Research*, *98*(B6), 9885–9907. Retrieved from http://doi.wiley.com/10.1029/93JB00191 doi: 10.1029/93JB00191

Rice, J. R., Lapusta, N., & Ranjith, K. (2001). Rate and state dependent friction and the stability of sliding between elastically deformable solids. *Journal of the Mechanics and Physics of Solids*, *49*, 1865–1898. Retrieved from http://linkinghub.elsevier.com/retrieve/pii/S0022509601000424 doi: 10.1016/S0022-5096(01)00042-4

Ruina, A. (1983). Slip instability and state variable friction laws. *Journal of Geophysical Research: Solid Earth*, *88*(B12), 10359–10370. Retrieved from http://doi.wiley.com/10.1029/JB088iB12p10359 doi: 10.1029/JB088iB12p10359